ANALYSIS OF A CANTILEVER BEAM TYPE VIBRATION ENERGY HARVESTER WITH A LEVER MECHANISM

by

Şeyda Ertarla

Submitted to Graduate School of Natural and Applied Sciences
in Partial Fulfillment of the Requirements
for the Degree of Master of Science in
Mechanical Engineering

Yeditepe University

2021

ANALYSIS OF A CANTILEVER BEAM TYPE VIBRATION ENERGY HARVESTER WITH A LEVER MECHANISM

APPROVED BY:

Assoc. Prof. Dr. Nezih Topaloğlu ……
(Thesis Supervisor)
(Yeditepe University)

Assoc. Prof. Dr. Mehmet Selçuk ARSLAN ……
(Yıldız Technical University)

Assist. Prof. Dr. Fethi Okyar ……
(Yeditepe University)

DATE OF APPROVAL: …./…./2021

ACKNOWLEDGEMENTS

I would like to express my very great gratitude to my advisor Assoc. Prof. Dr. Nezih Topaloğlu. His important advice helped me deal with critical points.

I would also thank to Volkan Karadağ with his grateful help.

Also, I would like to thank to TUBİTAK and Department of Mechanical Engineering for education and opportunity to complete my master degree.

ABSTRACT

ANALYSIS OF A CANTILEVER BEAM TYPE VIBRATION ENERGY HARVESTER WITH A LEVER MECHANISM

This thesis focuses on the energy harvesting efficiency of piezoelectric-based cantilever beam type vibration energy harvesters. The aim is to increase efficiency by homogenizing the axial stress along the beam. For this purpose, a counter mass is attached to the beam via a simple lever mechanism. This way, an inertial force is applied on the beam, having a direction opposite of the inertia force of the tip mass, thereby obtaining a loading close to pure moment. This structure is investigated in two methods; a detailed analytical model and numerical model are constructed. The analytical model and finite element analysis are used to assess the effect of two design parameters on efficiency, which are ratio of counter and tip masses, and lever beam length ratio. Modal analysis and harmonic response analyses are performed for both methods and compared with each other. The obtained results are compared with the strain distribution in a standard cantilever beam. It is shown that efficiency increases by means of the proposed method. As a result of analytical work, strain distribution greater than 0.53 was obtained. As a result of the test, strain distributions over 0.74 were obtained in a certain frequency bandwidth by altering with different mass and leverage ratios.

ÖZET

ANKANSTRE TİPİ TİTREŞİM KALDIRAÇ MEKANİZMALI ENERJİ DEPOLAYICISI ANALİZİ

Bu makale, piezoelektrik tabanlı ankastre kiriş tipi titreşim enerjili depolama makinelerinin enerji depolama verimliliğine odaklanmaktadır. Amaç, kiriş boyunca eksenel gerilimi homojenize ederek verimliliği artırmaktır. Bu amaçla, basit bir ankastre mekanizması ile kirişe bir karşı kütle tutturulur. Bu şekilde, kiriş üzerine, uç kütlenin eylemsizlik kuvvetinin tersi yönde bir eylemsizlik kuvveti uygulanır ve böylece saf momente yakın bir yükleme elde edilir. Bu yapı iki yöntemle incelenir; detaylı bir analitik model ve sayısal model oluşturulmuştur. Analitik model ve sonlu eleman analizi, iki tasarım parametresinin, karşı ve uç kütlelerinin oranına ve kaldıraç kiriş uzunluğu oranına dayalı olarak verimlilik üzerindeki etkisini değerlendirmek için kullanılır. Her iki yöntem için modal analiz ve harmonik yanıt analizi yapılır ve birbirleriyle karşılaştırılır. Elde edilen sonuçlar, standart bir kaldıraç kirişteki gerinim dağılımı ile karşılaştırılır. Önerilen yöntem sayesinde verimliliğin arttığı gösterilmiştir. Analitik çalışma sonucunda 0.53 ve üzeri gerinim dağılımı elde edilmiştir. Test sonucunda da farklı kütle ve kaldıraç oranlarıyla oynanılarak, belirli bir frekans aralığında 0.74 üzerinde gerinim dağılımları elde edilmiştir.

TABLE OF CONTENTS

LIST OF FIGURES

LIST OF TABLES

LIST OF SYMBOLS/ABBREVIATIONS

A	Cross sectional area
E	Elastic modulus
G	Gravity
H	Connecting beam
H_x, H_y	Point of revolute joint
I	Moment of inertia
L	Elastic beam
M	Tip mass
M'	Counter mass
M_v	Virtual mass
R_c	Updated version of the R_y
R_{dist}	Distributed harmonic force generated from the harmonic vibration of the distributed mass forming the beam
R_{tip}	Force consisting of the inertia of the tip mass
R_y, R_x	Vertical and horizontal force to be transferred to the elastic beam
y	Displacement relative to the beam root
y_t	Displacement of a point in the beam with respect to the ground
∅	Mode shape function
γ	Damping coefficient
B	Rotation angle of lever beam
P	Density
ω	Frequency

1. INTRODUCTION

1.1. AIM OF THE STUDY

Vibration energy harvesting research has been increased in recent years. Portable electronic devices, sensor networks, and body sensor networks can be shown as examples of applications of vibration energy harvesters (VEH). There are several methods to generate energy from vibration which are electromagnetism, electrostatics, and piezoelectricity.

Among vibration energy harvesting methods, piezoelectric cantilever beam is a trend topic. Mechanical energy which is a result of vibration is transduced into electrical energy by using a suitable circuitry if base excitation is applied to a piezoelectric unimorph or bimorph cantilever beam. Converting the strain on it into electrical displacement is a feature of piezoelectric material. Because of that, the harvested energy depends on the average stress or strain on the piezoelectric element which is on the cantilever beam surface. The surface stress will decrease linearly from the base to the tip which will be mainly in axial direction, when a static force is applied to the tip of a rectangular cantilever beam. Thus, the average stress on the beam surface is half of the maximum stress and base stress is an example of that.

Therefore, in energy harvesting, only half of the piezoelectric layer potential is used. There are numerous researches in order to increase the efficiency of piezoelectric-based cantilever beam VEHs. Generating more energy by obtaining uniform stress distribution along the beam is the objective. However, a small amount of improvement has been seen in many results aimed increase of stress distribution. Hence, some solution suggestions do not apply to standard piezoelectric beams.

1.2. LITERATURE SURVEY

There is considerable research on increasing the harvesting efficiency of piezoelectric-beam based vibration energy harvesters. Typical current and prospective applications of vibration energy harvesters (VEH) comprise wireless sensor networks, body sensor networks, implanted biomedical devices and portable electronics [1,2]. Three main transduction methods have been the focus of vibration energy harvesting research: electromagnetic [3], electrostatic [4] and piezoelectric [5].

There is a great effort on increasing the efficiency of piezoelectric-based cantilever beam VEHs. During vibration, voltage is generated on the piezoelectric layer at the surface of the beam, and this voltage is proportional to average axial stress on the beam surface [6]. In a typical cantilever beam with uniform width, the axial stress is maximum at the base of the cantilever beam and is close to zero at the beam tip [7]. This situation poses a serious limitation on the energy harvesting efficiency, due to the non-uniform stress distribution along the cantilever beam surface.

Kong et al. researched a microelectromechanical system piezoelectric cantilevered vibration energy harvester on c-axis tilted AlN thin film (Figure 1.1). Kong et al investigated geometry parameters effects and c-axis tilted angle effects. Kong et al produced micro-sized cantilever beams with piezoelectric thin films, at which the polarization of the piezoelectric layer is tilted from the out-of-plane direction [8]. Although this method increases the overall efficiency, it cannot be applied to batch fabricated piezoelectric patches. Introducing cavities into the beam cross-section also resulted in improved stress profile, but posed difficulty in fabrication [9,10].

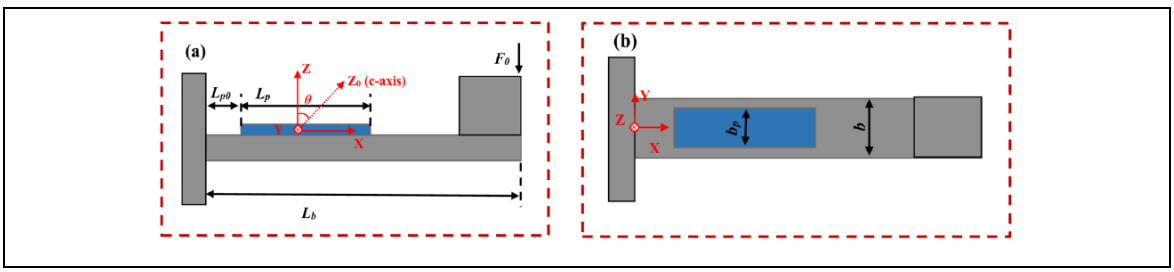

Figure 1.1. MEMS piezoelectric beam where the polorization axis makes an angle θ with the vertical axis: (a) side view, (b) top view [8]

A method which is piezoelectric energy harvester with multiple rectangular cavities at a single and two sections is built up by Raju et al who are researcher interested in cantilever piezoelectric energy harvesting. According to results of the research, two cavities result in producing maximum voltage and more voltage is generated with single cavity section if two cavity sections are compared. Yet, both methods are impractical [10].

Different piezoelectric beam shapes are investigated by Roundy et al. Using a varying beam width profile to improve stress distribution was first proposed by Roundy et al. It was suggested to use a tapered beam, i.e. a beam with linearly decreasing width profile from the base to the tip. Although more than twice the energy can be gained from a trapezoidal geometry than the rectangular geometry [7]. However, no theoretical or experimental study was presented. Recently, it was shown via theory [14,15], finite element analysis [16] and experiments [15] that tapered beams exhibit higher efficiency compared to beams with uniform width.

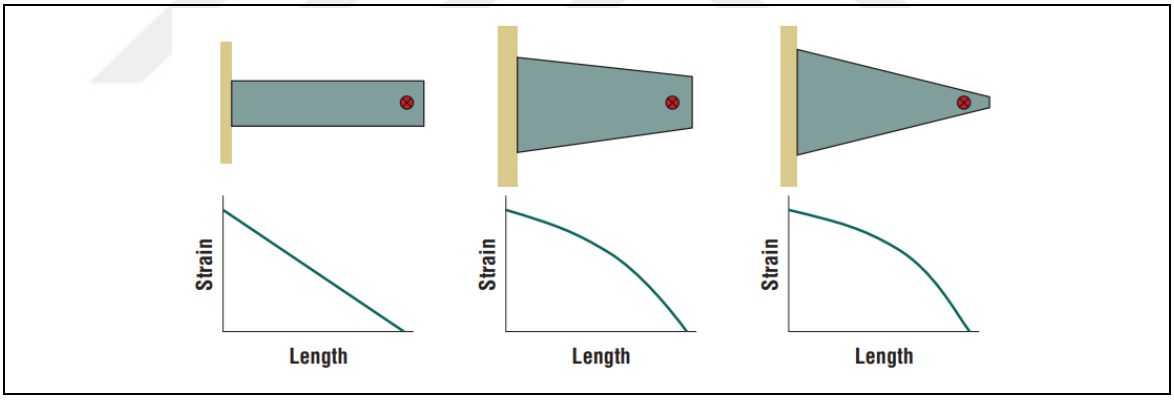

Figure 1.2. Strain profiles for different geometries [7]

In order to improve stress distribution along beam, a compliant hinge mechanism at the tip of cantilever beam is attached by Ma et al and proof mass is attached at the tip of the link (Figure 1.3). With the proposed mechanism, it has been possible to obtain a more homogeneous stress distribution on the beam surface by affecting the dynamic load at the beam end. As a result of the compliant mechanism at the tip, increases the tip displacement therefore large motion of the proof mass is produced [11].

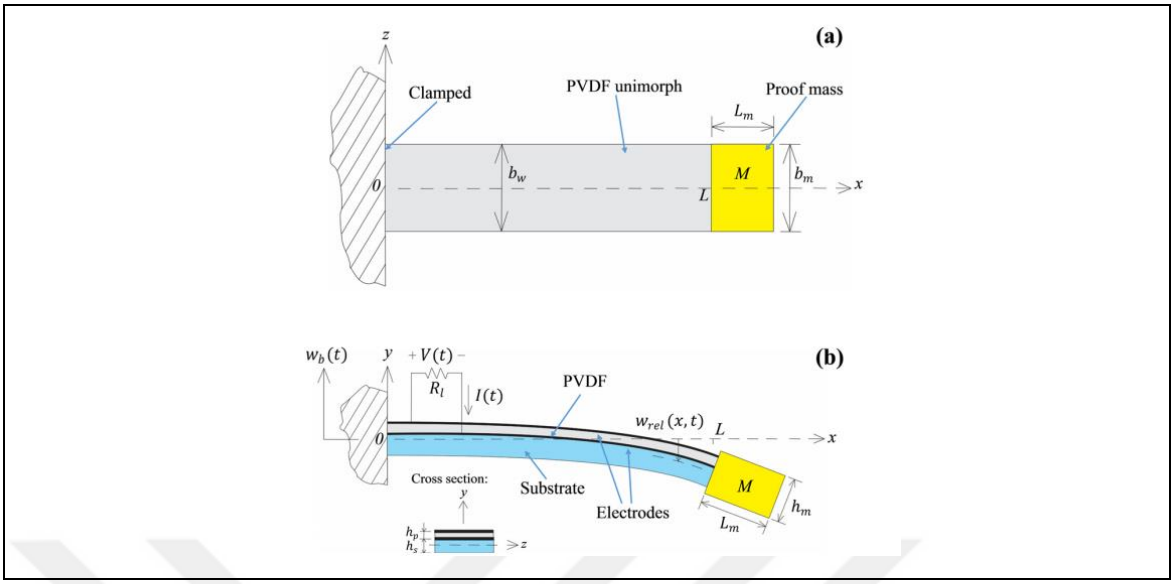

Figure 1.3. Cantilever beam with proff mass (a) Design and (b) Model [11].

Yoon et al investigated curved piezoceramic unimorphs' optimization in order to generate more charge as a result of mechanical loading (Figure 1.4). The response of a pre-stressed piezoelectric beam to vertical impact loads have been analyzed. In the research, PZT unimorph (lead zirconate titanate) structure is located as horizontal. This is because to generate surface charge when vertically loaded and to collect charge. However, generating energy from vibration is not sufficient in this methods due to applying pressure load which is applied on the top surface [12]. In a recent study, the stress distribution is homogenized by using a mechanical amplifier [13]. Both of these researches resulted in improved stress distribution, but the proposed devices are suitable to harvest energy only from impact type excitations.

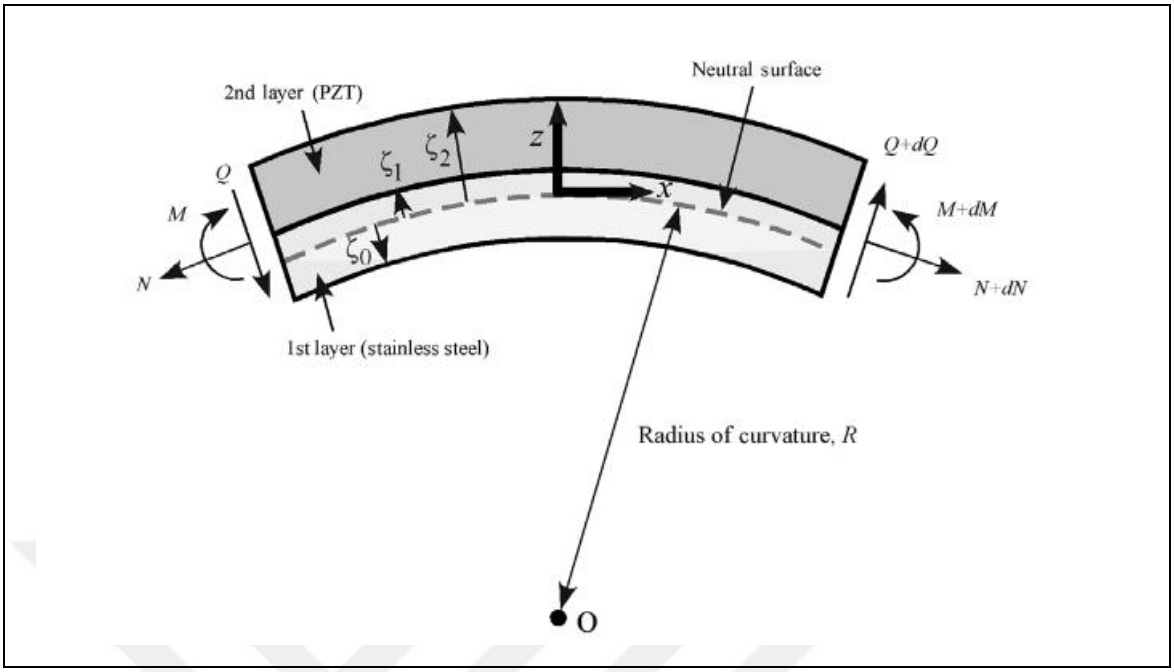

Figure 1.4. Pre-stressed piezoelectric energy generator [12]

Halvorsen et al analyzed and found out piezoelectric energy harvesters with tapered unimorph cantilever beams extended proof mass's models. This research includes long and short beam. The result of the work done to taper the beam does not conclude that it creates a more uniform stress. Also, there are no performance benefits when these harvesters are optimized for single frequency [14].

Tapered two-layer piezoelectric vibration energy harvesters are investigated by Xiong et al (Figure 1.5). While two masses are attached to each layer, base and upper cantilever beams are attached to each other. Due to change in masses positions, resonance frequencies can be generated by the convergent and divergent tapered harvesters [16].

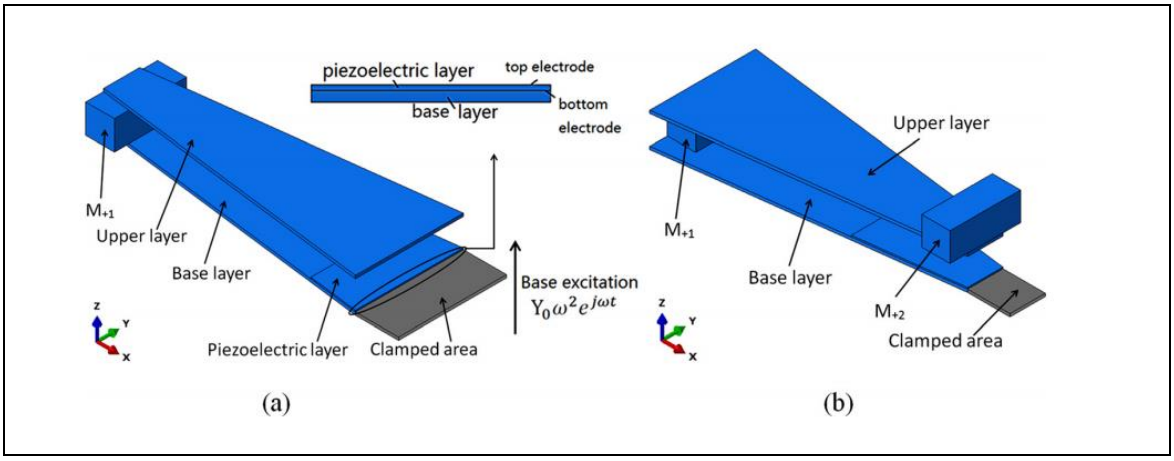

Figure 1.5. Piezoelectric beam generator (a) Two layer and one mass (b) Two layer and two masses [16].

Kianpoor et al also worked on energy harvesting which is from trapezoidal bimorph piezoelectric cantilever beams with proof mass. The research concluded that harvester's performance is excessively affected by geometrical parameters which are width, thickness, the dimensions of proof mass, and length of the beam. As a result of comparison of energy gains from direct and reverse trapezoidal and rectangle beams, more electrical power and voltage can be produced from the reverse trapezoidal geometry than other geometries [19].

To obtain more efficient piezoelectric energy harvesters, Hosseini et al studied on unimorph trapezoidal V-shaped cantilever beams. Triangular tapered cantilever beam, rectangular piezoelectric cantilever beam and trapezoidal V-shaped cantilever beam are compared for their energy efficiency. The study concluded that the deformation, strain and voltage of the triangular vibration energy collector are higher than the rectangular and trapezoidal beams.[20]

Hollow triangular piezoelectric cantilever beam harvesters by vibration to store more energy harvester is worked by Wang et al (Figure 1.6). A comparison of obtaining voltage from rectangular, trapezoidal, triangular, and hollow piezoelectric cantilever beams are made. A hollow triangular piezoelectric cantilever beam designed. Having more hollow in a beam result in more resonant frequency points, on the other hand, this leads to increase of length of substrate and beam's weight. As a result of that more deformation and fracture formed. New hollow triangular model which has no uniform thickness has varied resonant

frequencies. They are in the low frequency range broadens the resonance frequency bandwidth. However, production process of hollow cantilever beam is hard [21].

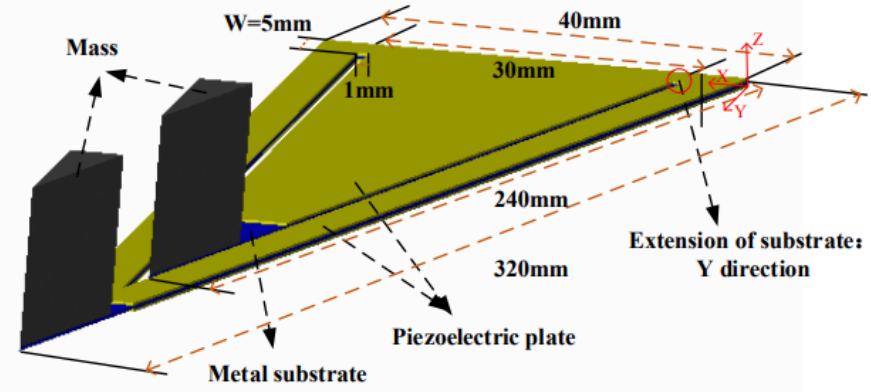

Figure 1.6. Hollow triangular piezoelectric [21]

Izadgoshasb studied on optimized shape of cantilever beam. The work aimed to increase performance of a Multiresonant Piezoelectric Energy Harvester (MRPEH) for low frequency vibrations. A cantilever beam which one piezoelecric patch attached to with two triangular brances and weight of tip mass consist of a model which is optimized by varying design parameters. Obtaining more energy with minimum weight of material and volume is the main aim of the research. As a result of the study overall efficiency of the MRPEH is higher tan the piezoelectric energy harvesters cantilever beams, it is independent of the excitation frequency [22].

C. V. Karadag study is about finding the optimal width profile for uniform strain distribution. Moreover, optimal width profile is affected by tip mass value which is a important parameter and there is no research on tip mass effect. Karadag et al in this study, a curved width profile is assumed and finite element based optimization is used to find optimized parameters for the highest strain uniformity. The optimized shapes, rectangular and triangular shapes were fabricated to compare stress distribution ratios and experimental results show that The stress distribution of the optimized-shaped beams are more than other convential beams [23].

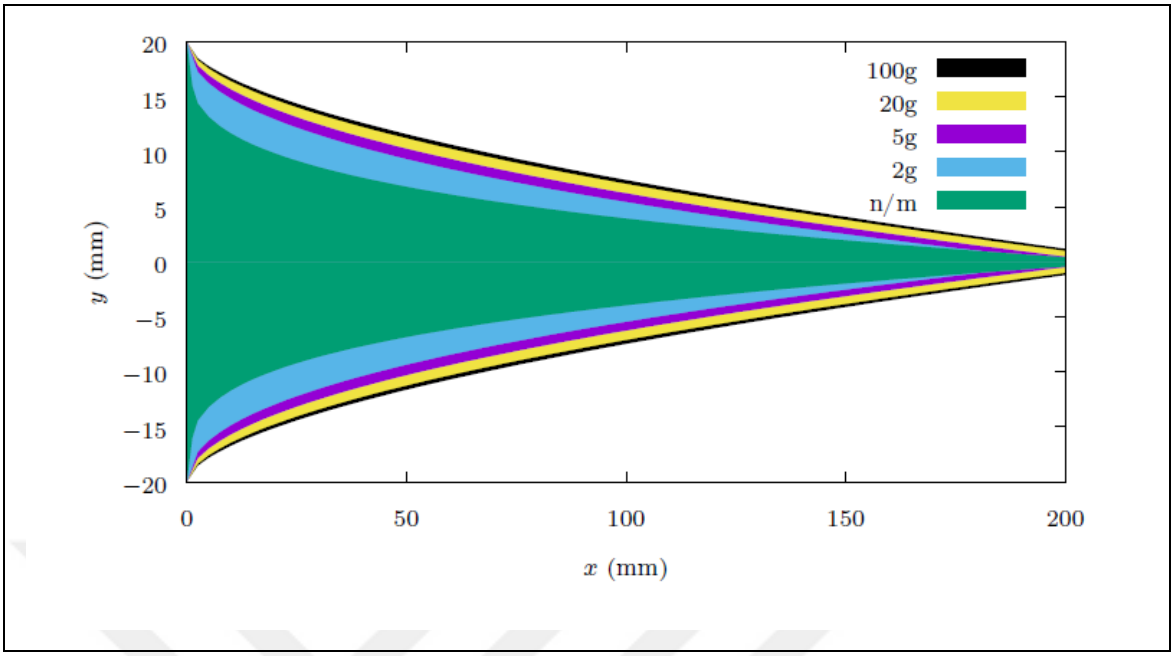

Figure 1.7. Optimization of width profile [23]

In this study a force, in opposite direction of inertial force due to tip mass motion, is applied to the beam during oscillation. Thus, it is aimed to obtain approximately a pure moment as the net load acting on the beam. Because of this, a counter mass is used with a simple lever mechanism, connected to the beam with a hinge. The inertial force affecting the counter mass is applied to the beam by changing direction, with the help of the lever mechanism. In this paper, a comprehensive analytical model of the proposed approach is explained and the preliminary results are presented.

2. PROPOSED METHOD

The main goal of the proposed method is to obtain a more uniform stress distribution on the cantilever beam during harmonic excitation. To achieve this goal, a counter mass is connected to the beam with a lever mechanism. The counter mass is located at the left end of the lever beam, and the other end of the lever beam is pin connected to a rigid link, which is pin-connected to the beam. The lever is also connected to the support with an L-shaped frame. A simple schematic of the mechanism is shown in Figure 2.1.

During oscillation, the inertia forces exerted by the tip mass and the counter mass will have the same direction (Figure 2.1). Due to the lever mechanism, the counter mass inertia force on the beam will have a direction opposite to the inertia force of the tip mass. This way, these two forces acting on the cantilever beam will have a moment effect, which in turn will result in a more uniform stress distribution on the beam.

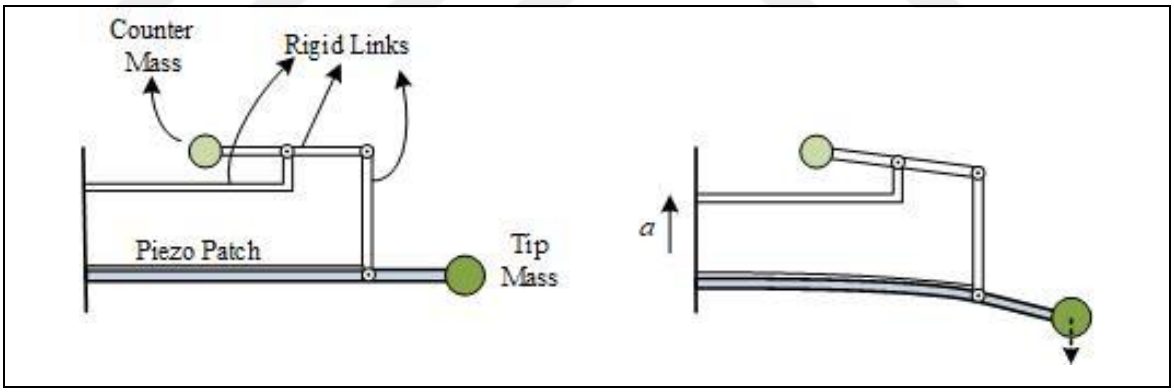

Figure 2.1. Concept of model

To assess the effect of geometrical parameters on the stress uniformity and demonstrate the improvement on stress uniformity with the proposed mechanism, a mathematical model is constructed, which is presented next.

2.1. RIGID BEAM MODEL- DETERMINATION OF OPTIMUM DIMENSIONS

L_1, L_2 and L_3 are determined as rigid beams that does not deform or change shape. L is flexible beam. of β is considered to be the small angle. The effect of horizontal force is neglected. The rigid beam that connects the lever is assumed to remain vertical during oscillation. The diagram below shows the oscillation image of the model at any moment.

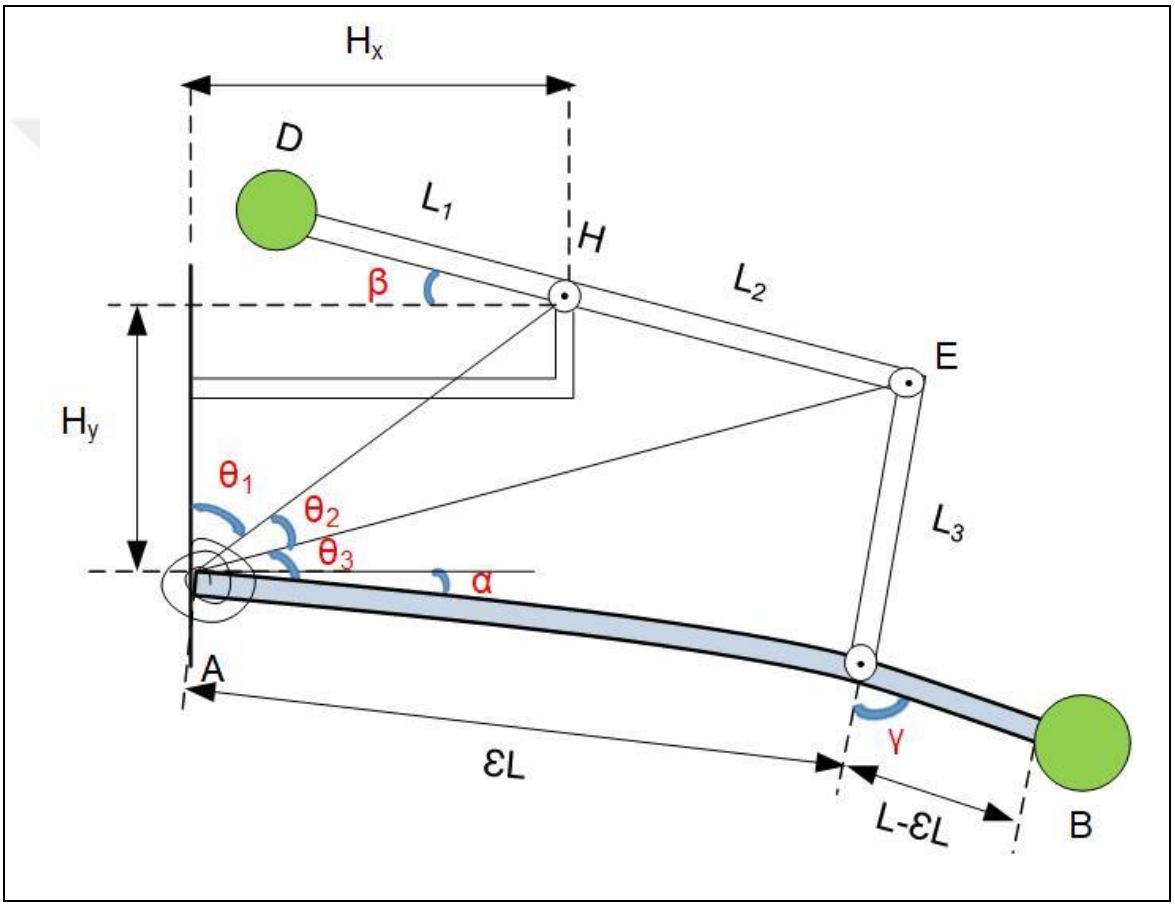

Figure 2.2. Kinematic scheme of model

2.1.1. Kinematic Solution

In the kinematic solution, the aim is to find the dimensions of the connecting beam perpendicular to the elastic and lever beam and to select the smallest H_y value within the perpendicularity limits.

Required lengths between angles and points are obtained by trigonometric calculations (Figure 2.2). In the following calculations are determined the positions and angles of model connection.

$$L_3 = \sqrt{{H_y}^2 + (H_x + L_2 - \varepsilon L)^2} \tag{2.1}$$

$$E_x = H_x + L_2 cos\beta \tag{2.2}$$

$$E_y = H_y - L_2 cos\beta \tag{2.3}$$

$$AE = \sqrt{{E_x}^2 + {E_y}^2} \tag{2.4}$$

Angles are found with trigonometric calculation:

$$\theta_1 = \tan^{-1}(\frac{H_x}{H_y}) \tag{2.5}$$

$$\theta_2 = \cos^{-1}\frac{(({H_x}^2 + {H_y}^2 + AE^2 - {L_2}^2)}{2AE\sqrt{({H_x}^2 + {H_y}^2}}) \tag{2.6}$$

$$\theta_3 = \cos^{-1}\frac{((AE^2 + \varepsilon L^2 - {L_3}^2)}{2AEeL}) \tag{2.7}$$

$$\gamma = \cos^{-1}\frac{({H_y}^2 + eL^2 - AE^2)}{2L_3\varepsilon L}) \tag{2.8}$$

$$\gamma_{angle} = \frac{180}{\pi}\gamma \tag{2.9}$$

$$\alpha = \theta_1 + \theta_2 + \theta_3 - \frac{\pi}{2} \tag{2.10}$$

Points are also calculated with trigonometric calculation:

$$A_x = 0 \tag{2.11}$$

$$A_y = 0 \tag{2.12}$$

$$B_x = Lcos\alpha \tag{2.13}$$

$$B_y = -Lsin\alpha \tag{2.14}$$

$$D_x = H_x - L_1 cos\beta \tag{2.15}$$

$$D_y = H_y + L_1 sin\beta \tag{2.16}$$

$$C_x = \varepsilon Lcos\alpha \tag{2.17}$$

$$C_y = -\varepsilon Lsin\alpha \tag{2.18}$$

Since the value of β is considered to be the small angle, it is considered to range between $\mp 20°$.

The default input parameter is below in mm:

Table 2.1. Input parameter (mm)

H_x	L	εL	L_1	L_2
60	120	100	40	40

In the graph of $90-\gamma$ vs β, 4 different H_y values (from 40 to 70 in 10 increments) are examined so that γ are as narrow angle range as possible.

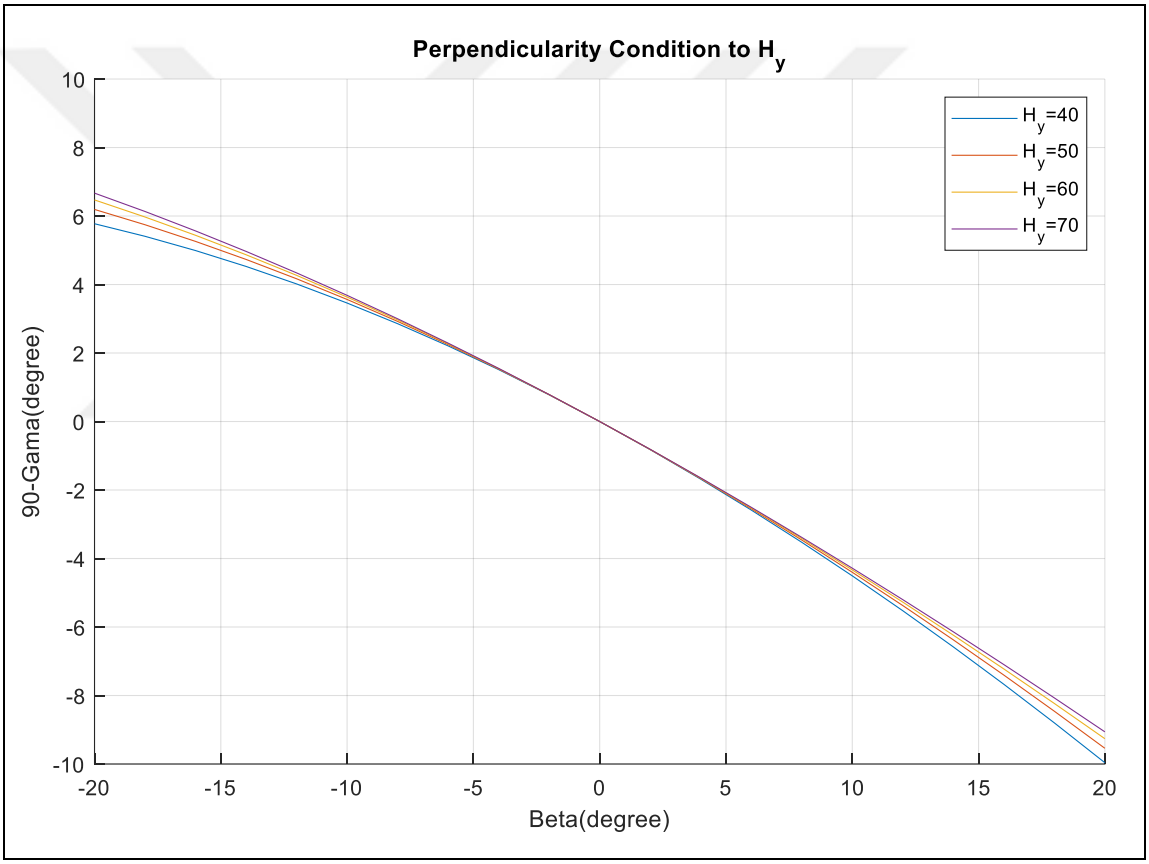

Figure 2.3. Perpendicularity condition to H_y

As the value of H_y increases, angle range of $90-\gamma$ in -20 to 20 decrease. H_y. In other words, When H_y is 40 mm , the range value is greater than H_y is 70 mm. That is, as the value of H_y increases, L_3 is considered perpendicular. However, smallest H_y value within the perpendicularity limits is 70 mm.

3. MATHEMATICAL MODELING

An extensive model of the proposed design is given in this section. The model includes the lever mechanism model, modal analysis of the beam and finally the harmonic response analysis based on modal expansion method.

Some assumptions are used to facilitate the modelling process; which are listed below:

- The piezoelectric beam is modelled using the Euler-Bernoulli beam theory, so the length to thickness ratio of the beam is assumed to be large. In addition, it is assumed that the beam consists of a single homogenous material. The effect of piezoelectric layer on beam response is neglected.
- The links that form the mechanism are assumed to be rigid and massless. All the joints that form the mechanism are assumed to be frictionless hinges. The tip mass and the counter mass are assumed to be point masses.
- The beam has rectangular cross section. Therefore, it is assumed that the stress on the beam does not vary in the z (i.e. width) direction.
- The damping on the beam is assumed to be viscous and to depend on the beam deflection rate with respect to the beam base. The damping effects on the lever mechanism are neglected.
- The rigid link that connects the lever to the beam is assumed to remain vertical during oscillation. As a result of this assumption, the force transmitted to the beam by this link will be in the transverse direction.
- The beam possesses small deformations, and the angle of rotation of the lever is assumed to be small.
- The stress induced on the beam in the static case is neglected.

3.1. MODELING OF THE LEVER MECHANISM

The model of the harvester, as can be remembered from Figure 2.1, consists of a flexible beam at the bottom, a connecting beam and a lever beam at the top. During vibration, it is aimed to transfer a force opposite to the inertia force of the tip mass to the harmonic beam with the help of the lever beam, so that the force applied to the harmonic beam from the tip reaches the pure moment.

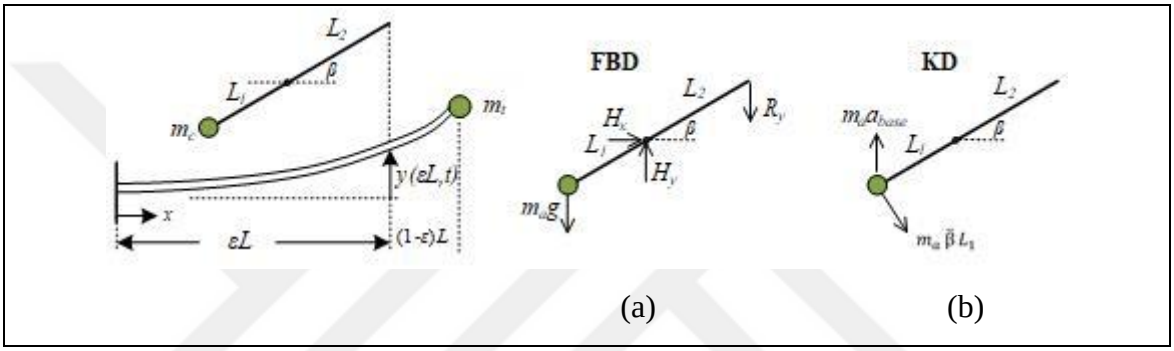

Figure 3.1. The design parameters of the lever and the beam (a); The free-body diagram (b) The kinetic diagram of the lever.

The mathematical model begins with the creation of free body and dynamic diagrams of the lever beam under harmonic vibration. It is assumed that both the lever beam and the connecting beam are weightless. Since the connector beam is a rigid element and only transfers forces, no diagram has been drawn for it. The free body and kinetic diagrams of the lever beam under harmonic base excitation are shown in Figure 3.1.

Determining force R_y is critical since the vertical force to be transferred to the elastic beam is R_y. The effect of force R_x is neglected since angle β is assumed small. The weight of counter mass is the only external force affecting the system in kinetic state. Centripetal and tangential accelerations create inertial force due to both vertical base excitation and the harmonic rotation of counter mass around point H.

In order to find force R_y, moment around point H , moment sum about H is taken both in the free-body and kinetic diagrams.

$$\circlearrowleft \sum M_H = \sum (M_H)_K \tag{3.1}$$

$$\cos\beta\left(M'gL_1 + R_yL_2\right) - R_xL_2 \sin\beta = -M'\left(\ddot{\beta}{L_1}^2\right) - M'(Y_0\omega^2\cos\omega t)L_1\cos\beta \tag{3.2}$$

Since angle β is assumed to be small, ($\cos\beta \sim 1$, $so\ \beta \sim 0$, $R_x \sim 0$), the moment equilibrium equation is re-arranged as follows.

$$M'gL_1 + R_yL_2 = -M'(Y_0\omega^2\cos\omega t)L_1 - M'\left(\ddot{\beta}{L_1}^2\right) \tag{3.3}$$

The following expression for R_y can be found.

$$R_y = \frac{L_1}{L_2}M'\left(-g - \ddot{\beta}L_1 - Y_0\omega^2\cos\omega t\right) \tag{3.4}$$

Assuming β to be small, R_y can be found.

$$\beta = y(\varepsilon L, t)/L_2 \tag{3.5}$$

$$\ddot{\beta} = \ddot{y}(\varepsilon L, t)/L_2 \tag{3.6}$$

$$R_y(t) = \frac{L_1}{L_2}M'\left(-g - Y_0\omega^2\cos\omega t - \ddot{y}(\varepsilon L, t)\frac{L_1}{L_2}\right) \tag{3.7}$$

R_y is the sum of three terms. The first term comes from the weight of the counter mass and it is neglected in the analysis since it has no dynamic effect on the system. The second term is proportional with base acceleration, and it can be modeled as harmonic external force. The third term is proportional with acceleration of elastic beam at point $x = \varepsilon L$. Using third term in the Euler-Bernoulli equation leaves the system insoluble. Therefore, in order to model third term, a virtual mass (M_v) is placed at $x = \varepsilon L$ on harmonic beam and the system can be solved. Now, R_y can be written as R'_y as shown below:

$$R'_y(t) = \frac{L_1}{L_2} M' Y_0 \omega^2 \cos \omega t \tag{3.8}$$

Finally, the value of the virtual mass located at $x = \varepsilon L$ should be:

$$M_v = (L_1/L_2)^2 M' \tag{3.9}$$

3.2. MODAL ANALYSIS

A simple representation of harmonic beam is shown in Figure 3.2. The force R'_y expressed in the previous section equation (3.8) affects x=εL. At the same point, there is the virtual mass, M_v expressed by equation (3.9). M represents the tip mass, L represents the length of the harmonic beam and y(t) represents the base excitation. Both tip mass and virtual mass are considered as point masses.

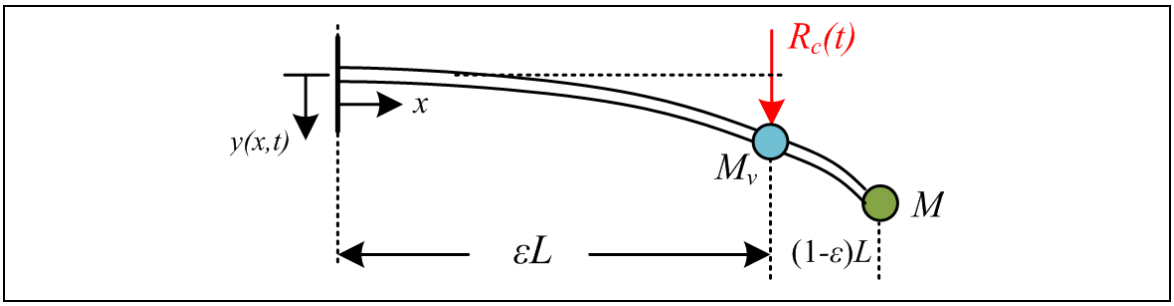

Figure 3.2. Simple representation of elastic beam

It can be said that the beam consists of two different parts (0<x<εL and εL<x<L) with different expressions of motion. The equation of motion is written for each piece based on the Euler-Bernoullli beam theory. Since modal analysis is performed, the equation of motion for free vibration and undamped state is written as:

$$EIy_i''''(x,t) + \rho A \ddot{y}_i(x,t) = 0\,, \quad i = 1,2 \tag{3.10}$$

The boundary conditions for both beam parts ($0 < x < \varepsilon L$ and $\varepsilon L < x < L$) are expressed as:

$$y_1(0,t) = 0 \tag{3.11}$$

$$y_1'(0,t) = 0 \tag{3.12}$$

$$\mathrm{EI}y_2''(L,t) = 0 \tag{3.13}$$

$$\mathrm{EI}y_2'''(L,t) = \mathrm{M}\ddot{y}_2(L,t) \tag{3.14}$$

Continuity conditions are expressed at the merged of the two parts:

$$y_1(\varepsilon L,t) = y_2(\varepsilon L,t) \tag{3.15}$$

$$y_1'(\varepsilon L,t) = y_2'(\varepsilon L,t) \tag{3.16}$$

$$y_1''(\varepsilon L,t) = y_2''(\varepsilon L,t) \tag{3.17}$$

$$\mathrm{EI}y_1'''(\varepsilon L,t) - M_v\ddot{y}(\varepsilon L,t) - \mathrm{EI}y_2'''(\varepsilon L,t) = 0 \tag{3.18}$$

The first three equations express a complete continuity due to unity of the beam. In the last equation, it is seen that the shear force changes due to the inertia effect of the virtual mass. With the method of separation of variables, the bending function for both parts is expressed as the product of temporal and spatial components.

$$y_i(x,t) = \emptyset_i(x)T_i(t) \tag{3.19}$$

In the above equation, *i* is the index expressing the part of the beam, the first part of the beam in case $i = 1$ expressed by $0 < x < \varepsilon L$, and in the case of $i = 2$, the second part of the beam is expressed by $\varepsilon L < x < L$. If the variable separation expressed by (3.19) is applied to the beam motion equation, the following expression is obtained.

$$\mathrm{EI}\emptyset_i''''(x)T_i(t) + \rho A\emptyset_i(x)\ddot{T}_i(t) = 0 \tag{3.20}$$

When the temporal and spatial components are separated, the following expression is obtained.

$$c^2 \ \frac{\emptyset_i''''(x)}{\emptyset_i(x)} = -\frac{\ddot{T}_i(t)}{T_i(t)} = \omega_i^2 \tag{3.21}$$

c denotes the wave velocity and is formulated as follows.

$$\mathrm{c} = \sqrt{EI/\rho A} \tag{3.22}$$

The spatial and temporal coordinate equations are written as follows.

$$\emptyset_i{}''''(x) - \beta_i^4\emptyset_i(x) = 0 \tag{3.23}$$

$$\ddot{T}_i(t) + \omega_i^2 T_i(t) = 0 \tag{3.24}$$

The relationship between β, ω and c is given below:

$$\beta_i^2 = \omega_i/c \tag{3.25}$$

The solution for (3.23) is given below:

$$\emptyset_1(x) = \ c_1\sin(\beta_1 x) + c_2\cos(\beta_1 x) + c_3\sinh(\beta_1 x) + c_4\cosh(\beta_1 x) \tag{3.26}$$

$$\emptyset_2(x) = c_5\sin(\beta_2 x) + c_6\cos(\beta_2 x) + c_7\sinh(\beta_2 x) + c_8\cosh(\beta_2 x) \tag{3.27}$$

The solution of the temporal equation (3.24) is as follows:

$$T_1(t) = E_1\cos(\omega_1 t) + F_1\sin(\omega_1 t) \tag{3.28}$$

$$T_2(t) = E_2\cos(\omega_2 t) + F_2\sin(\omega_2 t) \tag{3.29}$$

Boundary conditions given by (3.11)-(3.12) are rewritten with (3.19), (3.26), and (3.27).

$$c_2 + c_4 = 0 \tag{3.30}$$

$$c_1 + c_3 = 0 \tag{3.31}$$

$$-c_5\sin(\beta_2 L) - c_6\cos(\beta_2 L) + c_7\mathrm{sh}(\beta_2 L) + c_8\mathrm{ch}(\beta_2 L) = 0 \tag{3.32}$$

$$\begin{aligned} -c_5\cos(\beta_2 L) + c_6\sin(\beta_2 L) + c_7\mathrm{ch}(\beta_2 L) + c_8\mathrm{sh}(\beta_2 L) \\ = \frac{-\omega^2 M}{EI\beta_2^3}(c_5\sin(\beta_2 L) + c_6\cos(\beta_2 L) + c_7\mathrm{sh}(\beta_2 L) \\ + c_8\mathrm{ch}(\beta_2 L)\,) \end{aligned} \tag{3.33}$$

Here, *ch* and *sh* are used instead of *cosh* and *sinh* for abbreviation, respectively.

If the first of the continuity equations (3.15) is expressed again using temporal and spatial coordinates:

$$\emptyset_1(\varepsilon L)T_1(t) = \emptyset_2(\varepsilon L)\,T_2(t) \tag{3.34}$$

This equation can be valid for every t moment if the following condition is obtained.

$$T_1(t) = T_2(t) \tag{3.35}$$

In this case,

$$\emptyset_1(\varepsilon L) = \emptyset_2(\varepsilon L) \tag{3.36}$$

is obtained and thus it is concluded that the eigenvalues of the first and second part of the beam are the same.

$$\beta_1 = \beta_2 = \beta \tag{3.37}$$

$$\omega_1 = \omega_2 = \omega \tag{3.38}$$

Therefore, using the continuity equations (3.15)-(3.18) four new expressions given below in terms of the coefficient of the spatial function are obtained.

$$c_1\sin(\beta\varepsilon L) + c_2\cos(\beta\varepsilon L) + c_3\mathrm{sh}(\beta\varepsilon L) + c_4\mathrm{ch}(\beta\varepsilon L) = c_5\sin(\beta\varepsilon L) + c_6\cos(\beta\varepsilon L) + c_7\mathrm{sh}(\beta\varepsilon L) + c_8\mathrm{ch}(\beta\varepsilon L) \tag{3.39}$$

$$c_1\cos(\beta\varepsilon L) - c_2\sin(\beta\varepsilon L) + c_3\mathrm{ch}(\beta\varepsilon L) + c_4\mathrm{sh}(\beta\varepsilon L) = c_5\cos(\beta\varepsilon L) - c_6\sin(\beta\varepsilon L) + c_7\mathrm{ch}(\beta\varepsilon L) + c_8\mathrm{sh}(\beta\varepsilon L) \tag{3.40}$$

$$-c_1\sin(\beta\varepsilon L) - c_2\cos(\beta\varepsilon L) + c_3\sinh(\beta\varepsilon L) + c_4\cosh(\beta\varepsilon L) = -c_5\sin(\beta\varepsilon L) - \cos(\beta\varepsilon L) + c_7\mathrm{sh}(\beta\varepsilon L) + c_8\mathrm{ch}(\beta\varepsilon L) \tag{3.41}$$

$$-c_1\cos(\beta\varepsilon L) + c_2\sin(\beta\varepsilon L) + c_3\mathrm{ch}(\beta\varepsilon L) + c_4\mathrm{sh}(\beta\varepsilon L) + c_5\cos(\beta\varepsilon L) - c_6\sin(\beta\varepsilon L) - c_7\mathrm{ch}(\beta\varepsilon L) - c_8\mathrm{sh}(\beta\varepsilon L) = -\frac{\omega^2 M_v}{EI\beta^3}[c_1 sin(\beta\varepsilon L) + c_2 cos(\beta\varepsilon L) + c_3 sh(\beta\varepsilon L) + c_4 ch(\beta\varepsilon L)] \tag{3.42}$$

It is now possible to convert all these boundary condition and contunity equations into an eigenvalue problem expressed in matrix format.

$$\mathrm{A}\vec{\mathrm{x}} = \vec{b} \tag{3.43}$$

$$\vec{\mathrm{x}} = [c_1 \quad c_2 \quad \cdots \quad c_8]^T \tag{3.44}$$

$$\vec{\mathrm{b}} = [0 \quad 0 \quad \cdots \quad 0]^T \tag{3.45}$$

The following unitless states of the tip mass and virtual mass are used in matrix A.

$$A = \begin{bmatrix} 0 & 1 & 0 & 1 \\ 1 & 0 & 1 & 0 \\ 0 & 0 & 0 & 0 \\ 0 & 0 & 0 & 0 \\ sin(\beta\varepsilon L) & cos(\beta\varepsilon L) & sh(\beta\varepsilon L) & ch(\beta\varepsilon L) \\ cos(\beta\varepsilon L) & -sin(\beta\varepsilon L) & ch(\beta\varepsilon L) & sh(\beta\varepsilon L) \\ -sin(\beta\varepsilon L) & -cos(\beta\varepsilon L) & sh(\beta\varepsilon L) & ch(\beta\varepsilon L) \\ \beta L\underline{M}sin(\beta\varepsilon L) - cos(\beta\varepsilon L) & \beta L\underline{M}cos(\beta\varepsilon L) + sin(\beta\varepsilon L) & \beta L\underline{M}sh(\beta\varepsilon L) + cos(\beta\varepsilon L) & \beta L\underline{M}ch(\beta\varepsilon L) + sh(\beta\varepsilon L) \end{bmatrix} \cdots$$

(3.46)

$$\begin{bmatrix} 0 & 0 & 0 & 0 \\ 0 & 0 & 0 & 0 \\ -sin(\beta L) & -cos(\beta L) & sh(\beta L) & ch(\beta L) \\ \beta L\overline{M}sin(\beta L) - cos(\beta L) & \beta L\overline{M}cos(\beta L) + sin(\beta L) & \beta L\overline{M}sh(\beta L) + ch(\beta L) & \beta L\overline{M}ch(\beta L) + sh(\beta L) \\ -sin(\beta\varepsilon L) & -cos(\beta\varepsilon L) & -sh(\beta\varepsilon L) & -ch(\beta\varepsilon L) \\ -cos(\beta\varepsilon L) & sin(\beta\varepsilon L) & -ch(\beta\varepsilon L) & -sh(\beta\varepsilon L) \\ sin(\beta\varepsilon L) & cos(\beta\varepsilon L) & -sh(\beta\varepsilon L) & -ch(\beta\varepsilon L) \\ cos(\beta\varepsilon L) & -sin(\beta\varepsilon L) & -ch(\beta\varepsilon L) & -sh(\beta\varepsilon L) \end{bmatrix}$$

$$\overline{M} = Mc^2/EIL \tag{3.47}$$

$$\underline{M} = M_v c^2/EIL \tag{3.48}$$

The eigenvalues and eigenvectors of the system can be found when the determinant of matrix A is set to zero. The spatial function representing the mode shape number r, can be written in the following format:

$$\emptyset_{1r} = c_1 sin(\beta_r x) + c_2 cos(\beta_r x) + c_3 sh(\beta_r x) + c_4 ch(\beta_r x) \tag{3.49}$$

$$\emptyset_{2r} = c_5 sin(\beta_r x) + c_6 cos(\beta_r x) + c_7 sh(\beta_r x) + c_8 ch(\beta_r x) \tag{3.50}$$

The functions $\emptyset_{1r}$ and $\emptyset_{2r}$ here represent the mode shape of the r mode for the first and second part of the beam respectively. The Heaviside step function is used to express the rth mode shape of the whole beam with a single function.

$$\emptyset_r(x) = \emptyset_{1r}(x)[u(x) - u(x - \varepsilon L)] + \emptyset_{2r}(x)u(x - \varepsilon L) \tag{3.51}$$

The modal analysis is completed by finding the determinant of the A matrix numerically and equating it to zero and as a result finding the roots (β) and factors (c_i).

3.3. HARMONIC FREQUENCY RESPONSE

In this section, the response of the system to harmonic base excitation with the mode addition method has been found. It is assumed that the base excitation is harmonic and its amplitude

is $Y_0 \cos \omega t$. In the harmonic response analysis, the force applied to the harmonic beam by the connecting beam and the damping on the beam are included in the equation of motion. The equation of motion is given below:

$$EIy''''(x,t) + \rho A\ddot{y}_t(x,t) + \gamma\dot{y}(x,t) = F(x,t) \tag{3.52}$$

γ is damping coefficient, $y_t(x,t)$ represents the transverse displacement of a point in the beam with respect to the ground. The relationship between the beam displacement $y_t(x,t)$relative to the ground and displacement $y(x,t)$ relative to the beam root is given below:

$$y_t(x,t) = y(x,t) + Y_0 \cos\omega t \tag{3.53}$$

If the second derivative of the expression with respect to time is taken

$$\ddot{y}_t(x,t) = \ddot{y}(x,t) - Y_0\, \omega^2 \cos \omega t \tag{3.54}$$

When this expression is used in the equation of motion of the beam,

$$EIy''''(x,t) + \rho A\ddot{y}(x,t) + \gamma\dot{y}(x,t) = F(x,t) + R_{dist}(t) \tag{3.55}$$

In this equation, forces affecting the system externally are shown as $F(x,t)$

$$F(x,t) = R_c(t)\delta(x - \varepsilon L) + R_{tip}(t)\delta(x - L) \tag{3.56}$$

Two external forces act on the harmonic beam. One of them is the force ($R_c(t)$), acting by the connecting beam at the point $x = \varepsilon L$, and the other is the force ($R_{tip}(t)$) consisting of the inertia of the tip mass. $R_{dist}(t)$, shows the distributed harmonic force generated by the harmonic vibration of the distributed mass forming the beam.

$$R_{dist}(t) = \rho A Y_0 \omega^2 \cos \omega t \tag{3.57}$$

Before finding the $R_c(t)$ and $R_{tip}(t)$ forces, the processes to obtain harmonic response and the application of the orthogonality principle are shown. The harmonic function of the harmonic beam consists of the infinite sum of different mode responses. This sum where r index is the mod number is shown in the following equation:

$$y(x,t) = \sum_{r=1}^{\infty} \emptyset_r(x) T_r(t) \tag{3.58}$$

When this infinite sum is placed in the equation of motion (3.55), the following equation is obtained.

$$EI \sum \emptyset_r{}'''' T_r + \rho A \sum \emptyset_r \ddot{T}_r + \gamma \sum \emptyset_r \dot{T}_r = R_{dist}(t) + R_c(t)\, \delta(x - \varepsilon L) + R_{tip}(t)\, \delta(x - L) \tag{3.59}$$

In order to solve (3.59) it is necessary to eliminate the total symbol expressions and to benefit from the orthogonality condition.

Orthogonality application:

Since the modal shape function is a sum of trigonometric and hyperbolic terms, the following expressions can be easily obtained.

$$\emptyset_{1r}{}''''(x) = \beta_r{}^4 \emptyset_{1r}(x) \tag{3.60}$$

$$\emptyset_{2r}{}''''(x) = \beta_r{}^4 \emptyset_{2r}(x) \tag{3.61}$$

If two sides of (3.60) are multiplied by $\emptyset_{1s}$ and integral between$[0, \varepsilon L]$

$$\int_0^{\varepsilon L} \emptyset_{1r}{}'''' \emptyset_{1s}\, dx = \beta_r{}^4 \int_0^{\varepsilon L} \emptyset_{1r} \emptyset_{1s}\, dx \tag{3.62}$$

In this equation, partial integration is applied to the left side twice and the following equation is obtained.

$$\emptyset_{1s}(\varepsilon L)\emptyset_{1r}{}'''(\varepsilon L) - \emptyset'_{1s}(\varepsilon L)\emptyset_{1r}{}''(\varepsilon L) + \int_0^{\varepsilon L} \emptyset_{1r}{}''(x)\emptyset''_{1s}(x)\,dx = \beta_r{}^4 \int_0^{\varepsilon L} \emptyset_{1r}\emptyset_{1s}\,dx \tag{3.63}$$

When the same procedure is applied by changing the places of r and s modes, the following equation is obtained.

$$\emptyset_{1r}(\varepsilon L)\emptyset_{1s}{}'''(\varepsilon L) - \emptyset'_{1r}(\varepsilon L)\emptyset_{1s}{}''(\varepsilon L) + \int_0^{\varepsilon L} \emptyset_{1s}{}''(x)\emptyset''_{1r}(x)\,dx = \beta_s{}^4 \int_0^{\varepsilon L} \emptyset_{1s}\emptyset_{1r}\,dx \tag{3.64}$$

Then, (3.64) is subtracted from (3.63) and orthogonality condition is obtained for the first part of the beam.

$$\emptyset_{1s}(\varepsilon L)\emptyset_{1r}{}'''(\varepsilon L) - \emptyset'_{1s}(\varepsilon L)\emptyset_{1r}{}''(\varepsilon L) - \emptyset_{1r}(\varepsilon L)\emptyset_{1s}{}'''(\varepsilon L) + \emptyset'_{1r}(\varepsilon L)\emptyset_{1s}{}''(\varepsilon L) = (\beta_r{}^4 - \beta_s{}^4)\int_0^{\varepsilon L} \emptyset_{1s}\emptyset_{1r}\,dx \tag{3.65}$$

If the same operations are done for the second part of the beam, the following orthogonality condition is obtained.

$$\begin{aligned} -\emptyset_{2r}(L)\emptyset_{2s}{}'''(L) + \emptyset_{2s}(L)\emptyset_{2r}{}'''(L) - \emptyset'_{2s}(L)\emptyset_{2r}{}''(L) \\ + \emptyset'_{2r}(L)\emptyset_{2s}{}''(L) + \emptyset'_{2s}(\varepsilon L)\emptyset_{2r}{}''(\varepsilon L) \\ - \emptyset_{2s}(\varepsilon L)\emptyset_{2r}{}'''(\varepsilon L) + \emptyset_{2r}(\varepsilon L)\emptyset_{2s}{}'''(\varepsilon L) \\ - \emptyset'_{2r}(\varepsilon L)\emptyset_{2s}{}''(\varepsilon L) = \left(\beta_r{}^4 - \beta_s{}^4\right)\int_{\varepsilon L}^{L} \emptyset_{2r}\emptyset_{2s}\,dx \end{aligned} \tag{3.66}$$

When two orthogonality conditions are added together, the following equation is obtained.

$$\begin{aligned}&\Big(-\emptyset_{2r}(x)\emptyset_{2s}{}'''(x)+\ \emptyset_{2s}(x)\emptyset_{2r}{}'''(x)-\emptyset'_{2s}(x)\emptyset_{2r}{}''(x)\\&\qquad+\emptyset'_{2r}(x)\emptyset_{2s}{}''(x)\Big)_{x=L}\\&\qquad+\Big(\emptyset_{1s}(x)\emptyset_{1r}{}'''(x)-\emptyset'_{1s}(x)\emptyset_{1r}{}''(x)\\&\qquad-\emptyset_{1r}(x)\emptyset_{1s}{}'''(x)+\emptyset'_{1r}(x)\emptyset_{1s}{}''(x)\\&\qquad+\emptyset'_{2s}(x)\emptyset_{2r}{}''(x)-\emptyset_{2s}(x)\emptyset_{2r}{}'''(x)\\&\qquad+\emptyset_{2r}(x)\emptyset_{2s}{}'''(x)-\emptyset'_{2r}(x)\emptyset_{2s}{}''(x)\Big)_{x=\varepsilon L}\\&\qquad=(\beta_r^4-\beta_s^4)\left(\int_0^{\varepsilon L}\emptyset_{1s}\emptyset_{1r}\,dx+\int_{\varepsilon L}^{L}\emptyset_{2r}\emptyset_{2s}\,dx\right)\end{aligned}\tag{3.67}$$

Continuity and boundary conditions should be used to simplify this equation. When boundary conditions and continuity equations are applied, the following equation is obtained.

$$\left(\frac{M}{\rho A}\emptyset_{2r}(L)\emptyset_{2s}(L)+\frac{M_v}{\rho A}\emptyset_{1s}(\varepsilon L)\emptyset_{1r}(\varepsilon L)+\int_0^L\emptyset_s\emptyset_r\,dx\right)=\Psi\delta_{rs}\tag{3.68}$$

In this equation, Ψ_{rs} is an unknown constant, while the function δ_{rs} is 1 for $r=s$ and 0 for $r\neq s$.

$$\int_0^L\emptyset_s\emptyset_r\,dx=\Psi\delta_{rs}+\Omega_{rs}\tag{3.69}$$

$$\Omega_{rs}=-\left(\frac{M}{\rho A}\emptyset_{2r}(L)\emptyset_{2s}(L)+\frac{M_v}{\rho A}\emptyset_{1s}(\varepsilon L)\emptyset_{1r}(\varepsilon L)\right)\tag{3.70}$$

Complementary orthogonality conditions can also be written as follows.

$$\int_0^L\emptyset_r''''\emptyset_s\,dx=\beta_r^4\Psi\delta_{rs}+\Lambda_{rs}\tag{3.71}$$

$$\Lambda_{rs}=\emptyset_{1s}(\varepsilon L)\emptyset'''_{1r}(\varepsilon L)-\emptyset_{2s}(\varepsilon L)\emptyset'''_{2r}(\varepsilon L)+\emptyset_{2s}(L)\emptyset'''_{2r}(L)\tag{3.72}$$

$$\int_0^L \emptyset_r'' \emptyset_s'' \, dx = \beta_r^4 \Psi \delta_{rs} \tag{3.73}$$

In order to use the orthogonality equations in the equation of motion (3.59) it is necessary to multiply the equation by $\emptyset_s(x)$ and integrate it along the beam.

$$\begin{aligned} &\int_0^L EI \sum_{r=1}^{\infty} T_r \emptyset_r{}'''' \emptyset_s \, dx + \int_0^L \rho A \sum_{r=1}^{\infty} \emptyset_r \ddot{T}_r \emptyset_s dx \\ &\qquad = \int_0^L R_{dist}(t) \, \emptyset_s dx + \int_0^L R_c(t) \, \delta(x - \varepsilon L) \emptyset_s dx \\ &\qquad + \int_0^L R_{tip}(t) \, \delta(x - L) \emptyset_s dx \end{aligned} \tag{3.74}$$

As seen here, the damping part is not included in the equation. This part will be added to the equation when the temporal part will be found. The equation of motion becomes below, using the orthogonality equations.

$$\begin{aligned} &\sum_{r=1}^{\infty} EIT_r(\beta_r^4 \Psi \delta_{rs} + \Lambda_{rs}) + \sum_{r=1}^{\infty} \ddot{T}_r \rho A(\Psi \delta_{rs} + \Omega_{rs}) \\ &\qquad = \int_0^L R_{dist}(t) \, \emptyset_s dx + \int_0^L R_c(t) \, \delta(x - \epsilon L) \emptyset_s dx \\ &\qquad + \int_0^L R_{tip}(t) \, \delta(x - L) \emptyset_s dx \end{aligned} \tag{3.75}$$

If Λ_{rs} and Ω_{rs} expressions are put into the obtained equation, the following equation is obtained.

$$\sum_{r=1}^{\infty}\Big[-\ddot{T}_r\big(M\emptyset_{2r}(L)\emptyset_{2s}(L)+M_v\emptyset_{1s}(\varepsilon L)\emptyset_{1r}(\varepsilon L)\big) + EIT_r\big(\emptyset_{1s}(\varepsilon L)\emptyset'''_{1r}(\varepsilon L)-\emptyset_{2s}(\varepsilon L)\emptyset'''_{2r}(\varepsilon L) + \emptyset_{2s}(L)\emptyset'''_{2r}(L)\big)\Big] = \emptyset_s(\varepsilon L)\sum_{r=1}^{\infty}\Big[-\ddot{T}_r M_v\emptyset_{1r}(\varepsilon L) + EIT_r\big(\emptyset'''_{1r}(\varepsilon L)-\emptyset'''_{2r}(\varepsilon L)\big)\Big] + \emptyset_{2s}(L)\sum_{r=1}^{\infty}\Big[-\ddot{T}_r M\emptyset_{2r}(L)+EIT_r\emptyset'''_{2r}(L)\Big]=0 \tag{3.76}$$

Here, some terms are equal to zero due to boundary conditions and the following basic expression is obtained.

$$\left(\left(\frac{\rho A{\omega_s}^2}{EI}\right)EIT_s+\rho A\ddot{T}_s\right)\Psi = \int_0^L R_{dist}(t)\,\emptyset_s dx+\int_0^{\epsilon L}R_c(t)\,\delta(x-\epsilon L)\emptyset_s dx + \int_0^L R_{tip}(t)\,\delta(x-L)\emptyset_s dx \tag{3.77}$$

Integrals containing Dirac-Delta function on the right hand side of the equation can be found as follows.

$$\int_0^L \delta(x-\varepsilon L)\emptyset_s dx=\emptyset_s(\varepsilon L) \tag{3.78}$$

$$\int_0^L \delta(x-L)\emptyset_s dx=\emptyset_s(L) \tag{3.79}$$

For the integral of the mode shape along the beam, the function $\emptyset_{int}$ is defined.

$$\emptyset_{int} = \int_0^L \emptyset_s dx \tag{3.80}$$

To solve (3.77) , $R_{tip}(t)$ and $R_c(t)$) must be determined. (For $R_{dist}(t)$ see (3.57). $R_{tip}(t)$ is the inertia force seen in the tip mass as a result of the harmonic base excitation and is expressed as

$$R_{tip}(t) = MY_0\,\omega^2 \cos\omega t \tag{3.81}$$

Another inertia force will be seen in the virtual mass at connecting point and will form a component of $R_c(t)$. The other component of $R_c(t)$ is the harmonic force applied by the lever.

This force was found in (3.8) as $R'_y(t)$. In this case, $R_c(t)$ expression will be as follows.

$$R_c(t) = \frac{L_1}{L_2} M' Y_0 \omega^2 \cos(\omega t)\left(\frac{L_1}{L_2} - 1\right) \tag{3.82}$$

In this case, adding the damping, the following equation is obtained.

$$\begin{aligned} EI\beta_s{}^4 T_s(t) + \frac{\gamma}{\rho A}\dot{T}_s(t) + \ddot{T}_s(t) \\ = \frac{Y_0\omega^2 \cos\omega t}{\rho A \Psi}\left(\rho A \emptyset_{int} + \emptyset_s(\epsilon L)\frac{L_1}{L_2} M'\left(\frac{L_1}{L_2} - 1\right)\right. \\ \left. + \emptyset_s(L) M\right) \end{aligned} \tag{3.83}$$

The steady-state response can be obtained as;

$$\begin{aligned} T_s(t) = \frac{Y_0\omega^2\left[\rho A \emptyset_{int} + \emptyset_s(\epsilon L)\frac{L_1}{L_2} M'\left(\frac{L_1}{L_2} - 1\right) + \emptyset_s(L) M\right]}{\rho A \Psi \sqrt{(\omega_s^2 - \omega^2)^2 + (2\zeta_s\omega_s\omega)^2}} \cos(\omega t \\ - \theta_s) \end{aligned} \tag{3.84}$$

$$\theta_s = \tan^{-1} \frac{2\zeta_s \omega_s \omega}{\omega_s^2 - \omega^2} \tag{3.85}$$

$$\zeta_s = \gamma / 2\rho A \omega_s \tag{3.86}$$

Finally, as written in equation 8, to obtain the bending function of the beam, $T_s(t)$ is multiplied by $\emptyset_s(x)$ given in (3.51) and the infinite mode sum is made.

$$y(x,t) = \sum \emptyset_s(x) T_s(t) \tag{3.87}$$

4. FINITE ELEMENT METHOD

Finite Element analysis program (FEAP) is used to verify the analytical model computations.

The advantages of Finite Element Analysis Program (FEAP) are listed below:

- Feap is open source software.
- Matlab interface to FEAP is proper.
- It is possible to obtain stress distribution per node on the beam surface.

4.1. MODELING

The modal and harmonic analysis is performed in the FEAP program. The raw data obtained with FEAP was transferred to MATLAB in Paraview (VTU) format, the next operations are performed in MATLAB.

In the finite element model (FEM), all beams are modeled using a three-dimensional shell element. The reason for choosing a shell element is as follows: Since the thickness (2 mm) to length (200 mm) ratio in the beams is low, the transverse shear deformation is negligible. If three dimensional solid elements were used, it would be necessary to use very small size elements in order to keep the width, height and height of the elements close to each other. As a result, the number of elements that creates the mesh would have increased significantly.

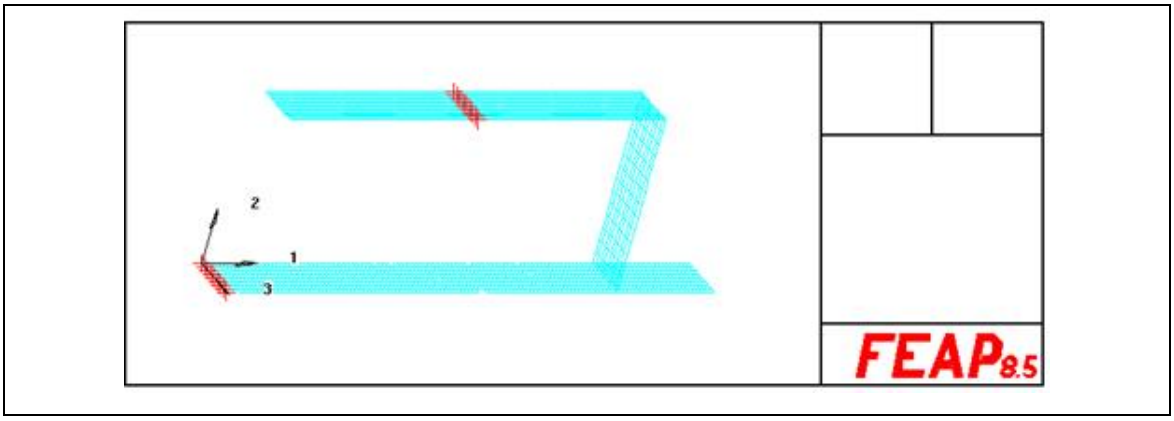

Figure 4.1. FEM mesh of the model

Aluminum material is used for the elastic beam (elastic modulus 69 GPa, density 2.7 g / cm3, Poisson's ratio 0.33) and very high elastic modulus and very low density for the lever and connecting beams to meet the weightless and rigid condition in the analytical model. (elastic modulus 2100 GPa, density 7.8e-3 g / cm3, Poisson ratio 0.29) The aim here is to prevent the lever and connecting beam from flexing and to try to impart pure moment effect only to the base beam. The boundary condition in the base beam is cantilever beam. In order to achieve this, nodes are restricted in 1 and 2 directions shown in Figure 4.1. Since applying restriction in excess direction while applying the boundary condition will cause rigidity of the system and locally high stresses, only one node in the direction 3 is restricted and the others are released. In addition, rotational movements in both direction 1, 2 and 3 are restricted.

At the support point of the lever beam, it is necessary to apply a boundary condition to reveal the rotary joint. For this purpose, translation movement in direction 1 and 2 is restricted in all nodes shown in red in the lever beam in Figure 4.1. In the direction 3, only one node is restricted and the other nodes are released. In order to give this limit a rotational joint feature, no restriction in the direction of rotation in direction 3 is applied to any node. The rotation in the other two directions is completely restricted. To see how these boundary conditions are applied in the FEAP environment, the annotated code dumps in Appendix A can be viewed.

In order to realize the rotary joint or hinge-like connections between the beams, all the joints at the edges where the connecting beam intersects with the elastic beam and the lever beam are associated with the LINK command. In order for both connections to act as hinges, 3

directions of the displacement axes are kept closed. 1-way rotation axis is limited and 2-way and 3-way rotation axes are released. The reason for the release of the 2-way rotation axis is to make the model less rigid, preventing its natural frequency from increasing, and preventing local high stresses from occurring.

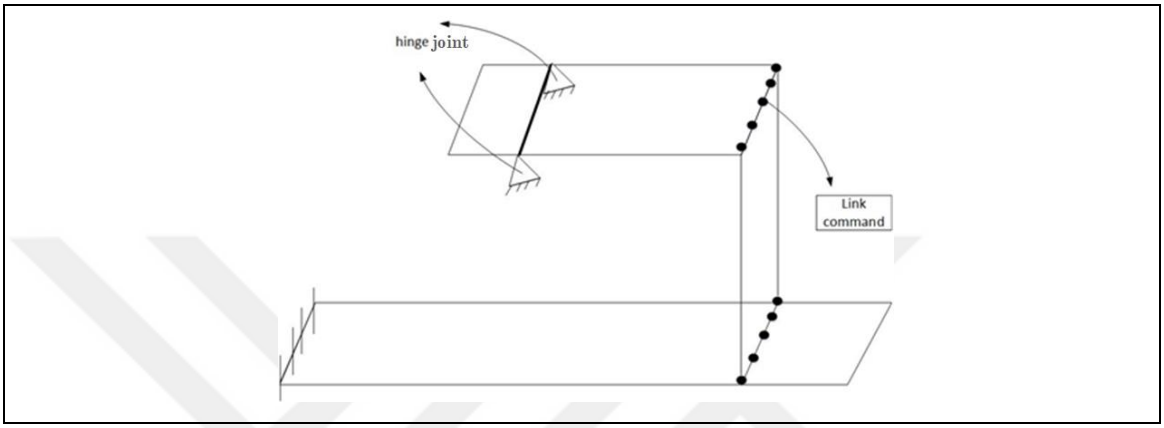

Figure 4.2. Link Command- connection point

The tip mass and the counter mass are placed in the form of point masses at the end middle node of the base beam and lever beam in order not to disturb the symmetry. The locations of these nodes are given in Figure 4.2.

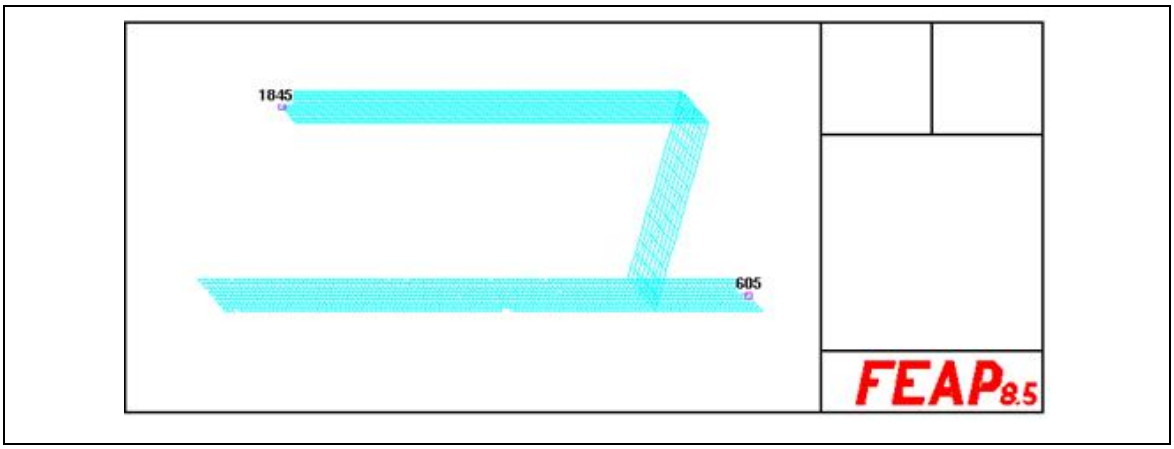

Figure 4.3. Nodes with tip and counter mass in FEM

After the meshing process is completed, modal and harmonic analysis is performed. In modal analysis, eigenvalues and eigenvectors are calculated and natural frequency and mode shapes are obtained. Figure 4.4 shows the first and second mode shape obtained for an example configuration (M'/M = 0.5 and L_1/L_2= 1). When the first mode shape is examined (Figure 4.4(a)), the right end of the base beam moves upward in the direction of 2, while the left end of the lever beam moves downward. The connecting beam is also raised. This shows that the system is modeled correctly and the initial mode shape is as expected. The second mode figure is seen in Figure 4.4(b). The natural frequency of both modes is indicated below the corresponding Figure 4.4.

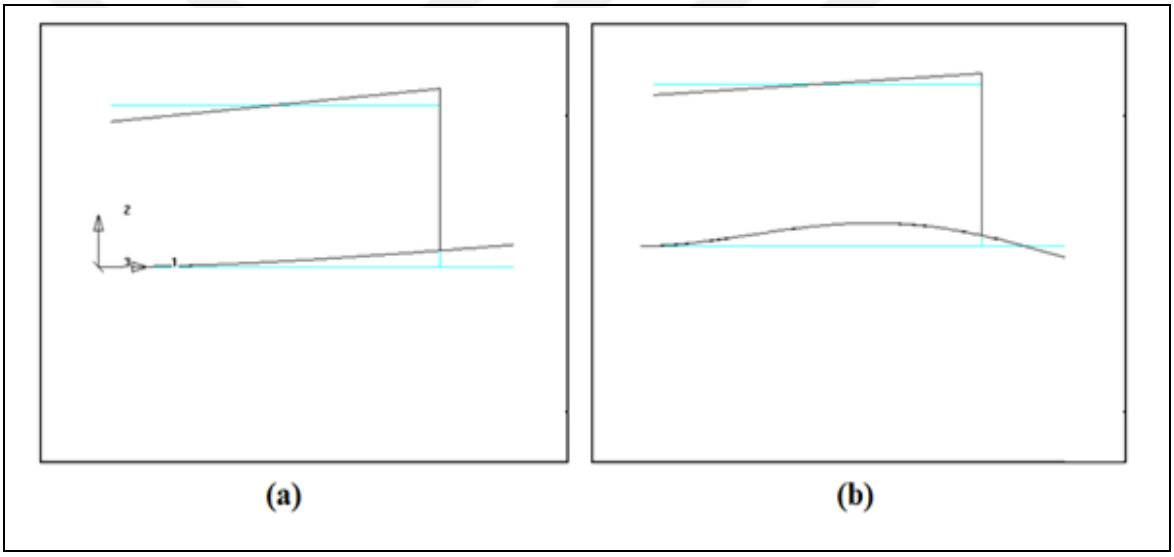

Figure 4.4. Mod shapes obtained by FEM (a) First mod shape (b) Second mod shape.

In harmonic analysis, the system is subjected to 1 mm amplitude harmonic base excitation. Using the CXSOLVE command, the frequency range and damping ratio are entered, and the displacement and stresses of the harmonic system are calculated. In the example given in Figure 4.5, the system is shaken at a frequency close to its natural frequency. The light blue figure shows the position of the undeformed beam. The amount of displacement caused by the base excitation appears as a contour. In this analysis, the maximum displacement is negative since the end of the elastic beam moves downward. Regions with boundary condition (yellow colored) appear about 1 mm. This result shows that the analysis works as expected, since the base excitation given to the system is 1 mm.

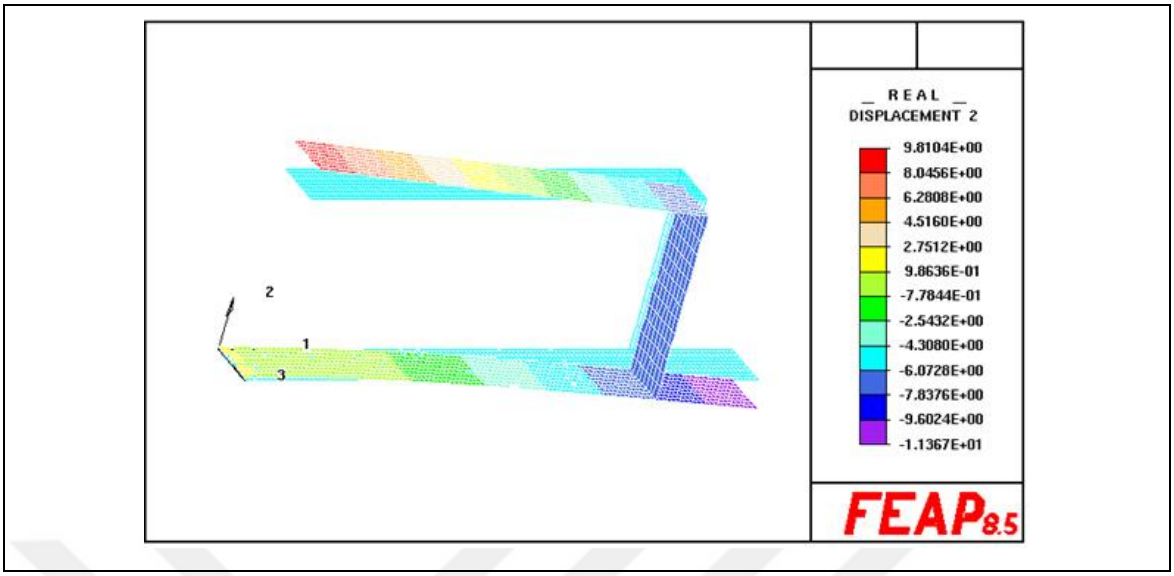

Figure 4.5. Sample harmonic analysis result node displacements

It is more convenient to perform the necessary operations to calculate the strain distribution in MATLAB. Therefore, node positions, displacements, and stresses for each frequency are saved in the VTU file format. Then, saved VTU files are opened with MATLAB and variables are defined in MATLAB environment. The MATLAB code performing this process can be seen in Appendix A. Graphical representation of the finite element model results is given Figure 4.6. Here, the blue color shows the displacement and the colored contour image shows the axial strain. As a result of the analysis, the stress and position values at the nodes on the elastic beam surface are used and the strain distribution is calculated using the (Figure 4.7).

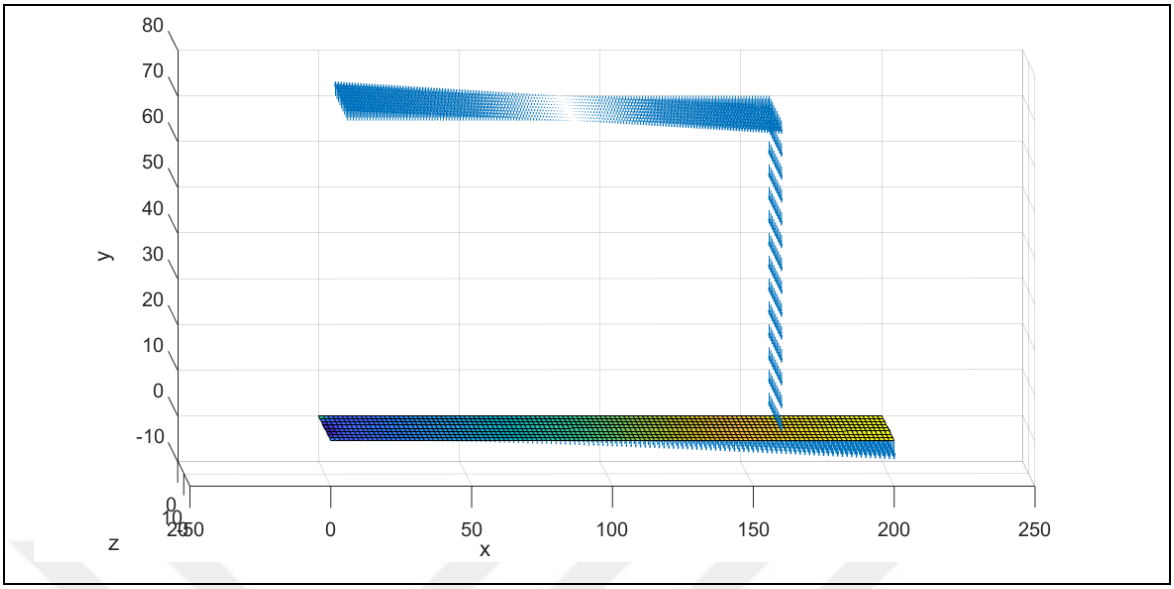

Figure 4.6. Representation of FEM results for the model in Matlab

The strain distribution parameter is found in MATLAB using the position (x, y) and axial strain values for each node on the beam surface. The strain distribution is equal to the average axial strain in the beam surface area divided by the peak strain value. The challenge is to calculate the average axial strain across the surface. A geometric method is used for calculating the average strain. Here, the horizontal axes show the position (x, y) of the node point on the beam surface, while the vertical axis is the strain value of the related node. In this case, the average strain distribution in the quadrilateral consisting of the nodes (x_1, y_1), (x_2, y_2), (x_3, y_3) and (x_4, y_4) is that the volume of the polyhedra in Figure 4.7 is equal to the surface area of the quadrant formed by the nodes. The strain distribution is calculated by applying this geometric method to every four adjacent nodes.

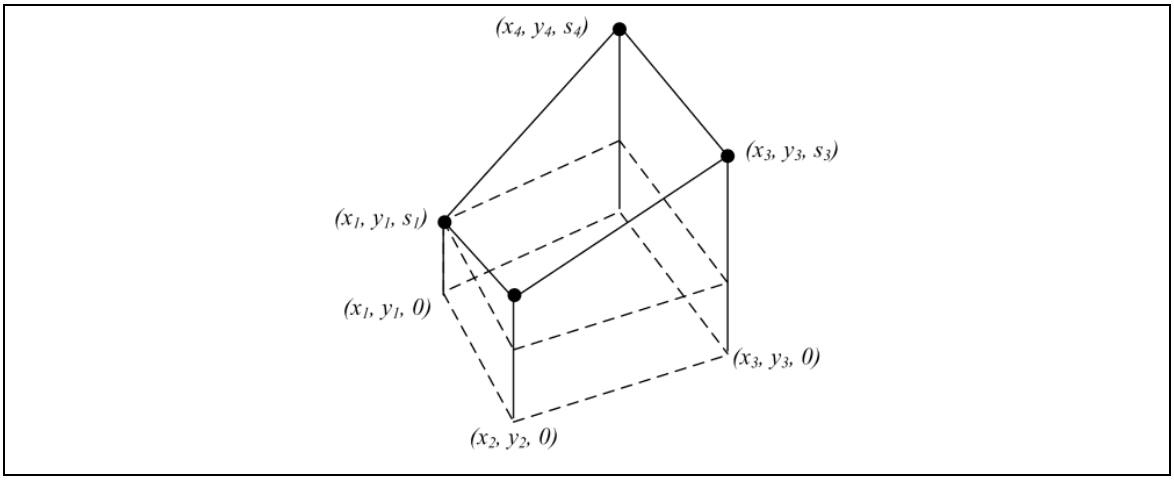

Figure 4.7. Beam surface area average strain calculation method

4.2. FEM SOFTWARE AND VERIFICATION

Before I model proposed method, known cantilever beam with tip force is modelled to FEAP program in both statics and complex forms in order to compare and verify with mathematical model.

4.2.1. Basic Mathematical Model

End Load On Cantilever Beam.

Cantilever beam acts as a spring under force, Figure 4.8 shows beam deflection

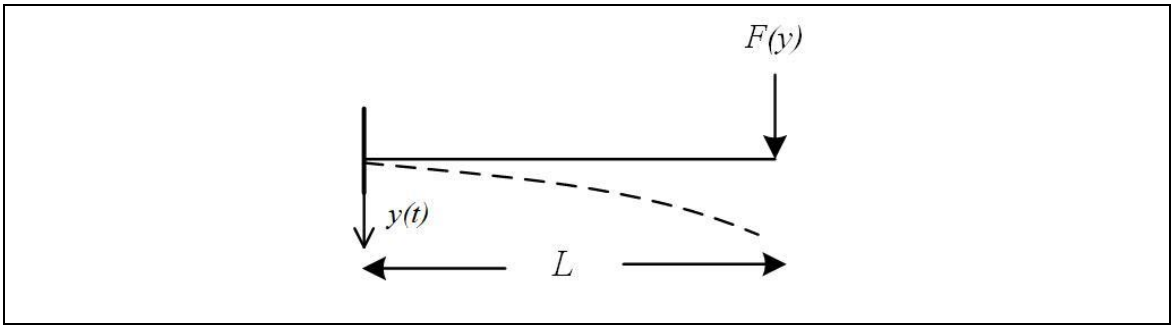

Figure 4.8. Tip deflection of cantilever beam

According to Euler-Bernoulli Beam Theory, tip deflection is found by following equation:

$$y = \frac{FL^3}{3EI} \tag{4.1}$$

Cantilever beam is modelled with below parameters.

Table 4.1. Geometric parameters

Geometric Parameters (mm)		
b (width)	h (thickness)	L (Length)
20	2	100

Table 4.2. Young's modulus, density, Poisson ratio

E(GPa)	ρ(kg/m^3)	ν
69	2700	0.33

Moment of inertia is found with below equation:

$$I = \frac{1}{12} bh^3 \tag{4.2}$$

Transverse tip force is determined as F is 10 kN

4.2.2. Verification of Feap

Before I model proposed method, known cantilever beam with tip force (see code form in Appendix A) is modelled to FEAP program in order to compare and verify with mathematical model. Analysis is done for transverse tip force in Y direction. Transverse force, F is 10 kN are determined.

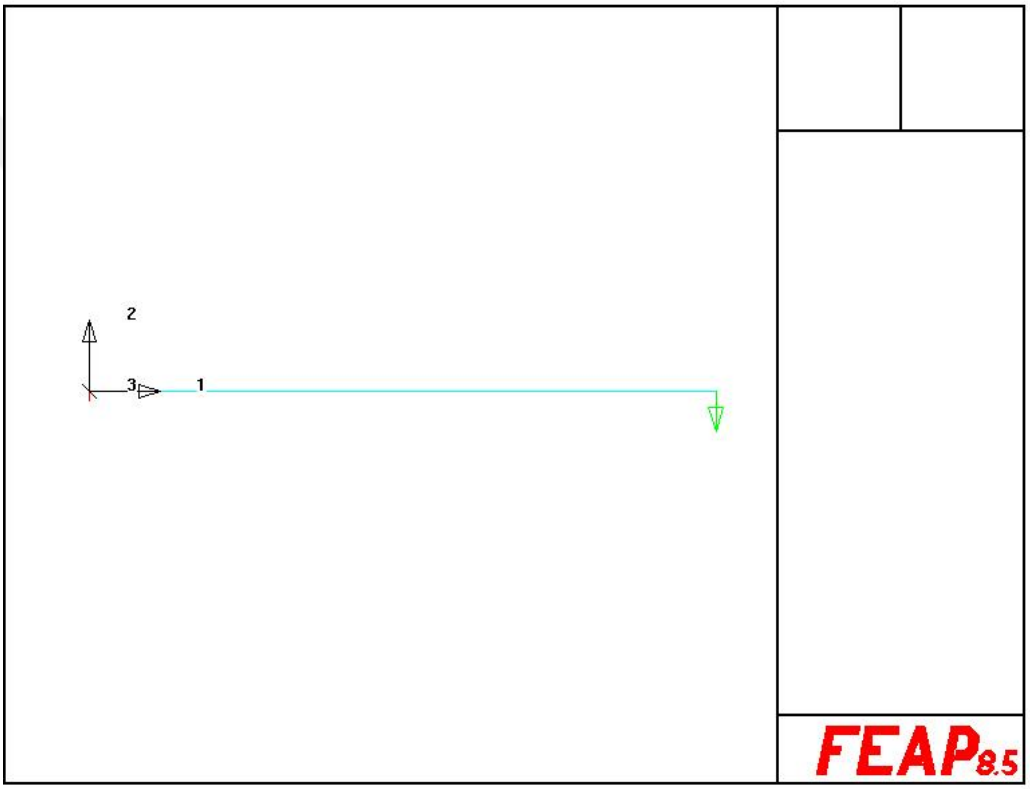

Figure 4.9. Feap statics analysis of tip deflection of cantilever beam

All models, tip force location are determined at middle point of tip of beam. While maximum deflection is 3.6231 mm in the analytical model, and 3.5348 mm in feap statics.

Table 4.3. Comparison of theory and FEM

Analytics	Feap Statics
3.6231 mm	3.5348 mm

5. COMPARISON OF METHODS

In order to compare the finite element model (FEM) results with the analytical model, firstly, fundamental natural frequency values in different design parameters are compared. These results can be seen in Figure 5.1. As can be seen, FEM results and analytical model results are very close. Also, as expected, both the increase in lever ratio and the increase in dimensionless mass cause a decrease in natural frequency; because in both cases the equivalent inertia of the system increases.

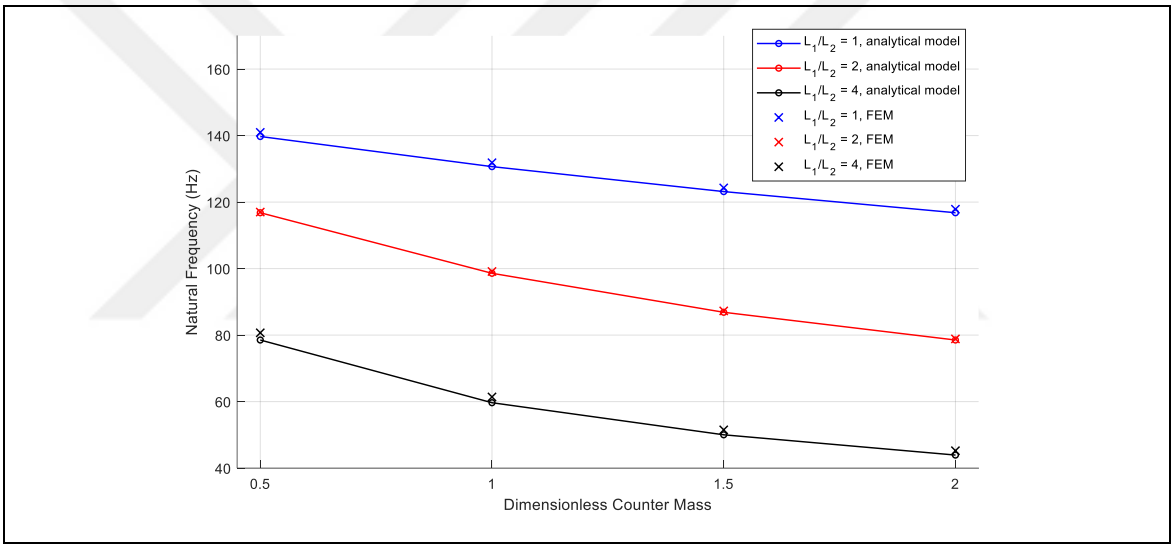

Figure 5.1. Analytical model and FEM comparison

Another parameter for analytical model and FEM comparison is the frequency response of the tip mass in the harmonic beam obtained as a result of harmonic analysis. As can be seen, FEM and analytical model results are compatible with each other. Also, analytical model and FEM comparison is made in cases where the leverage ratio is greater than one. These results are given in Figure 5.2, Figure 5.3 and Figure 5.4 for the cases where leverage ratio 1, 2 and 4 respectively. It is seen that the differences between results become significant, especially when the leverage ratio is increased. When the differences between the finite element model and the analytical model are examined, it is seen that the finite element model is made using shell elements and includes high deformation. In the analytical model, Euler-

Bernoulli beam theory is used and it is accepted that the beam deformations are low. In addition, it is assumed that the connecting beam is always vertical and does not transmit horizontal force to the harmonic beam. It is assumed that the angle β formed by the horizontal beam of the lever beam during vibration is small and small angle approach is made while writing the equation of motion. As a result of all these, it is thought that there are differences between the analytical model and FEM. Another important point is that while the natural frequencies obtained as a result of modal analysis are very close to each other, the difference is in the harmonic response analysis. While the modal analysis module in the FEAP program is a stable module developed a long time ago, the complex solution (CXSOLVE) module used for harmonic response is a module still under development. Especially, problems were experienced in the operation of LINK command, which provides the connection between beams, with CXSOLVE, and the problems were solved by getting support from the developers in the user forum of the FEAP software. This situation is thought to be the cause in the harmonic response analysis and the strain distribution results obtained from it compared to the analytical model.

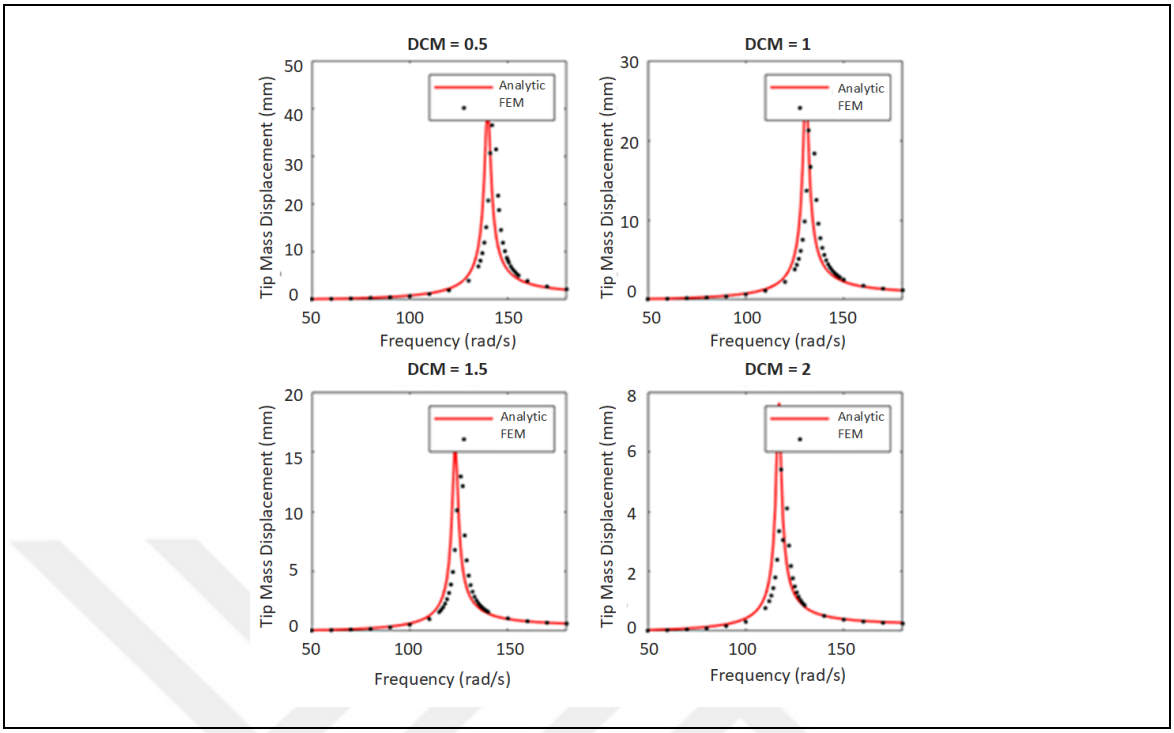

Figure 5.2. Comparison of analytical and FEM for $\boldsymbol{L_1/L_2 = 1}$

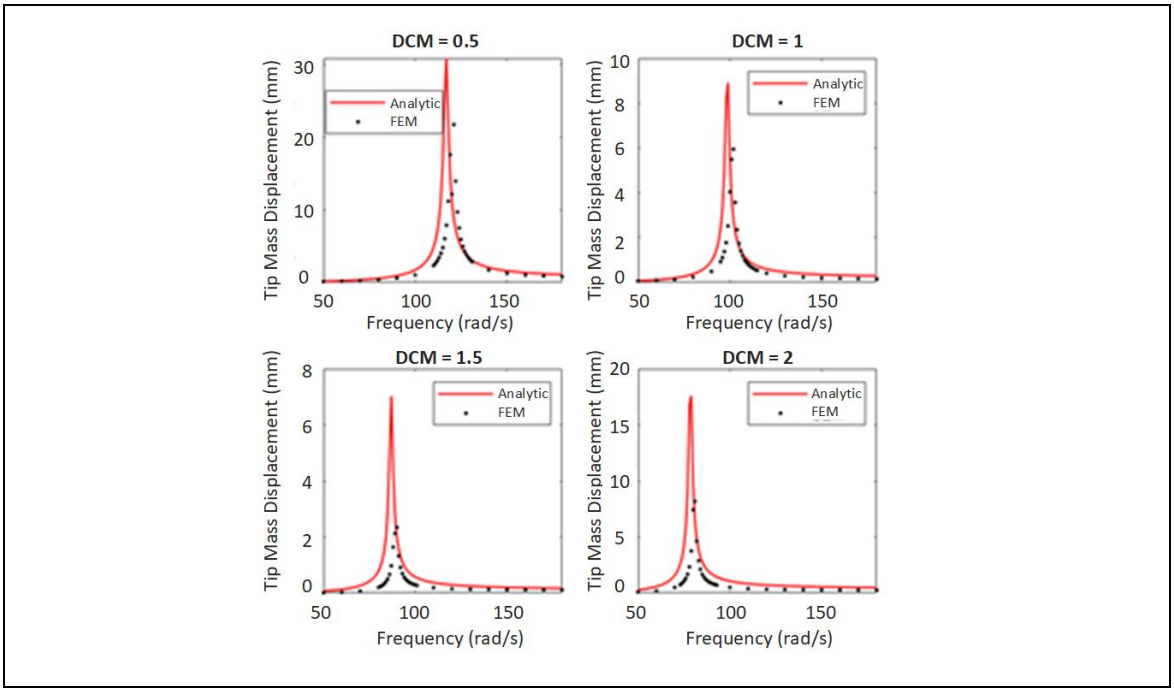

Figure 5.3. Comparison of analytical and FEM for $L_1/L_2 = 2$

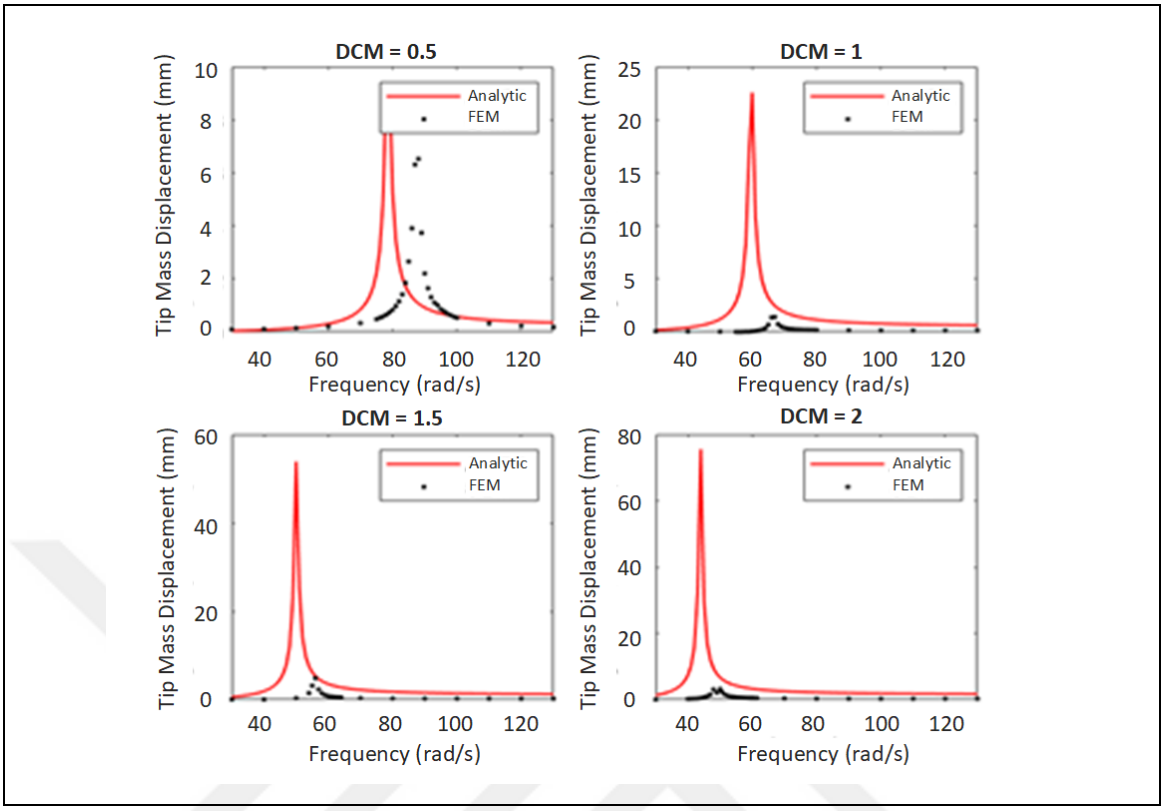

Figure 5.4. Comparison of analytical and FEM for $L_1/L_2 = 4$

In this way that the legend on the left graph is valid for all three graphs, the analytical model is given in a wide dimensionless frequency range, while the finite element model is run around resonance. Here, it is seen that the strain distribution obtained by analytical model is slightly higher than the finite element model. This difference is thought to be due to differences in the harmonic response analysis results. In addition, numerical errors can be seen in the strain distribution calculation with FEM, since the curve fitting to the deflection data depending on the position in the beam and then the second derivation of the obtained deflection equation are performed. One of the reasons for the high failure of the strain distribution obtained by finite element analysis is that the average strain is divided by the maximum strain in the strain distribution formula. In finite element analysis, strain values can increase significantly, especially in the root parts where stiffness is high. It is thought that this will cause a decrease in the strain distribution. For all these reasons, the analysis of high strain distribution continues using the analytical model.

Examples have been made to see the strain change from root to tip. For DCM and leverage ratio are 1, system is excited to 138 rad/sec that is near to excitation frequency value (105 percent). DCM 0.5 and leverage ratio are 1, system is excited to 150.15 rad/sec that is near to excitation frequency value (105 percent). For DCM 1.5 and leverage ratio are 1, system is excited to 131.25 rad/sec that is near to excitation frequency value (105 percent). The nodes in the midpoint where the beam will be along a line from root to tip were viewed. Aim is to examine strain value change from root parts to tip. It is seen that strain decreases from root to tip. (Figure 5.5). The variation of the root to tip strain at the midpoint node is shown in the graphs respectively (Figure 5.6, Figure 5.7 and Figure 5.8). While there is a decrease in the strain from the root to the tip in the graph, a jump is observed at the point where the connecting beam is connected to the base beam in the model (160 mm). It is observed that the strain suddenly increases as the root of the beam is approached. In this situation, this will cause a decrease in the strain distribution. As an example if we assume that the strain does not make a sudden change at the root of the beam (as shown by the red dashed line), then for Figure 5.6 strain distribution will increase from 0.46 to 0.57. If a same update is performed for Figure 5.7 and Figure 5.8. New strain values will be from 0.46 to 0.58 and from 0.45 to 0.56. This values are closer to the analytical results.

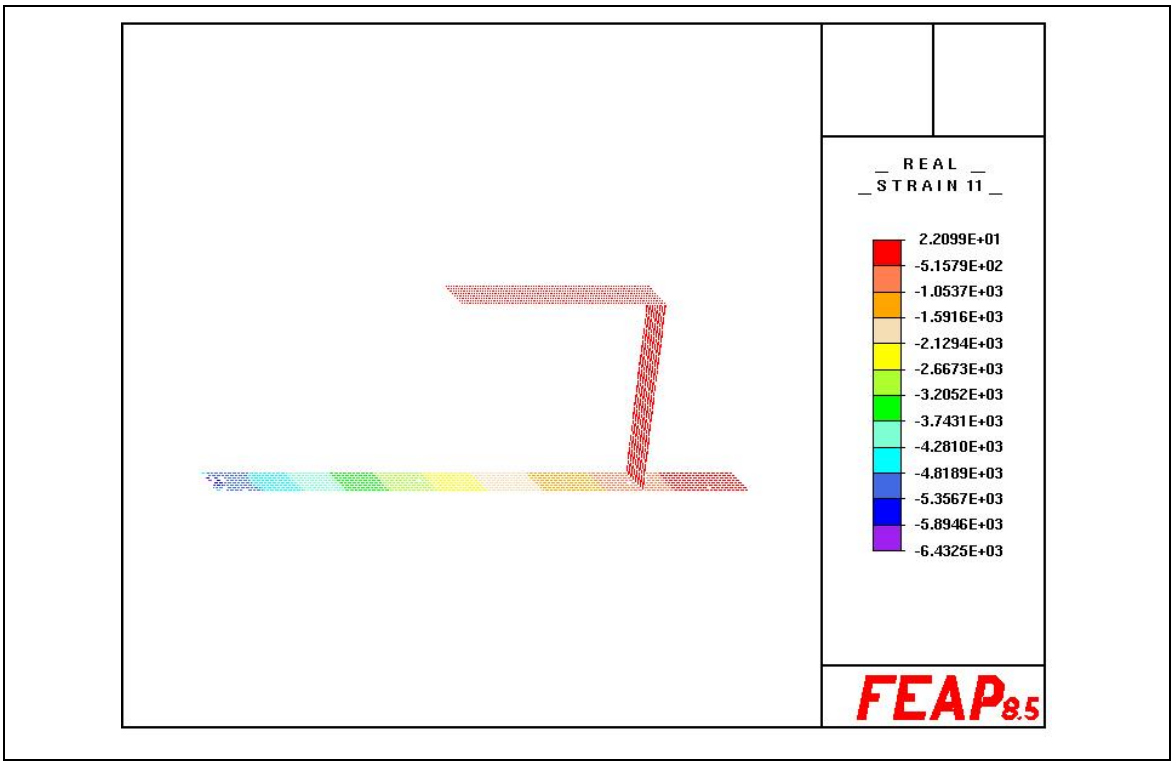

Figure 5.5. Strain graph for FEM of the model for DCM and leverage ratio are 1

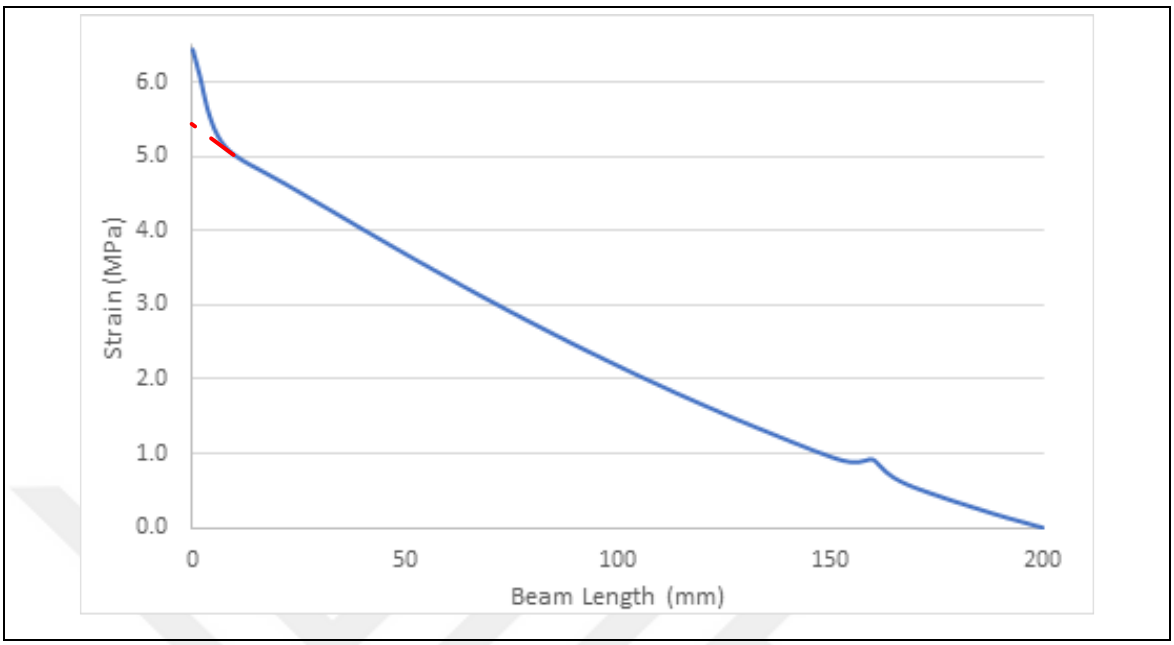

Figure 5.6. Strain change along the beam for $(\boldsymbol{M' / M = 1})$ and $(\boldsymbol{L_1/L_2 = 1})$

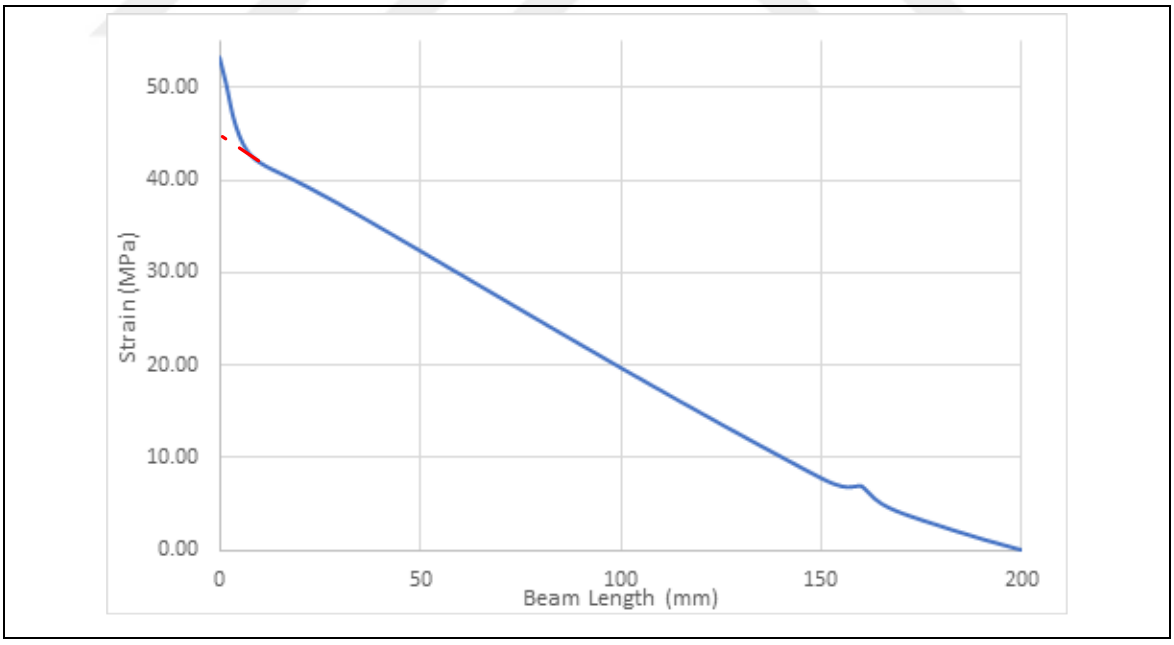

Figure 5.7. Strain change along the beam for $(\boldsymbol{M' / M = 0,5})$ and $(\boldsymbol{L_1/L_2 = 1})$

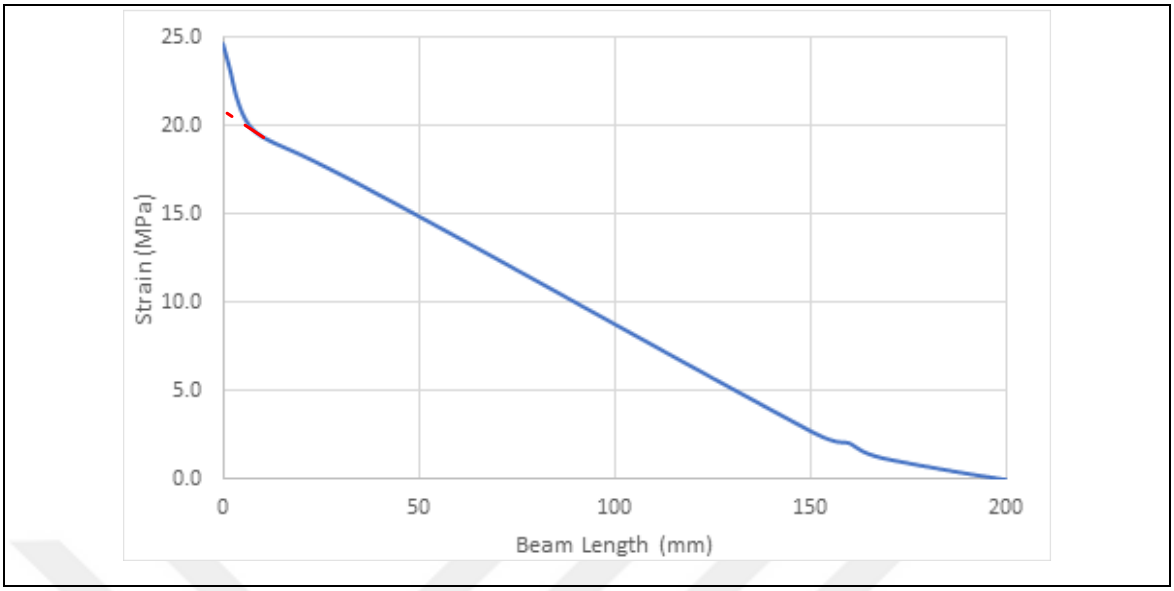

Figure 5.8. Strain change along the beam for $(\boldsymbol{M' / M = 1, 5})$ and $(\boldsymbol{L_1/L_2 = 1})$

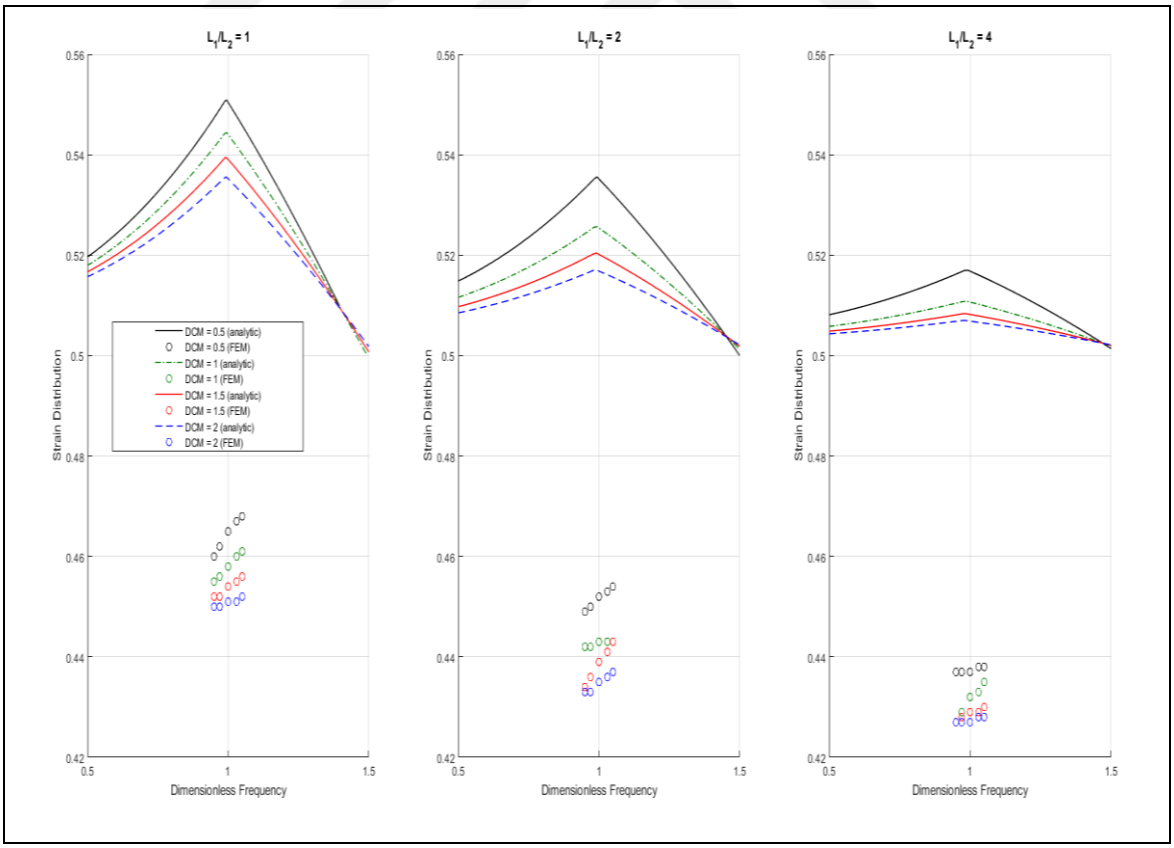

Figure 5.9. Strain distributions for analytical model and FEM of the model

In order to obtain a high strain distribution, a load close to the inertial load that the tip mass creates on the beam must be created by the counter mass. It is obvious that both the dimensionless counter-mass and the leverage ratio values are important for this. However, in the experimental study, it is not practical to adjust the leverage ratio precisely because it is necessary to produce a new leverage, hence the experimental setup, for each new leverage ratio experiment. However, it is possibe to precisely adjust the counter mass with nuts attached to a bolt. For this reason, the analytical model is used again to obtain high strain distribution by changing the dimensionless counter mass precisely and for three different leverage ratios (0.5, 1, and 2), the frequency response of the strain distribution is found by changing the DCM precision. Results are given in Figure 5.10, Figure 5.11 and Figure 5.12.

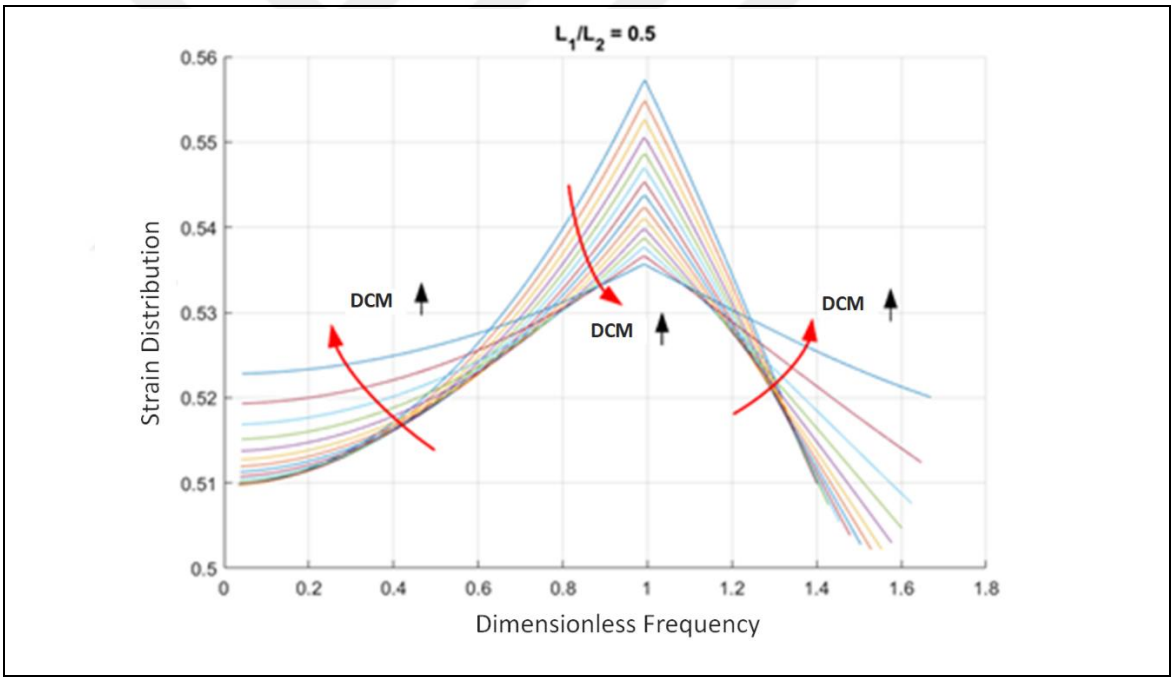

Figure 5.10. Strain distribution when DCM is fine-tuned for $\boldsymbol{L_1/L_2 = 0.5}$

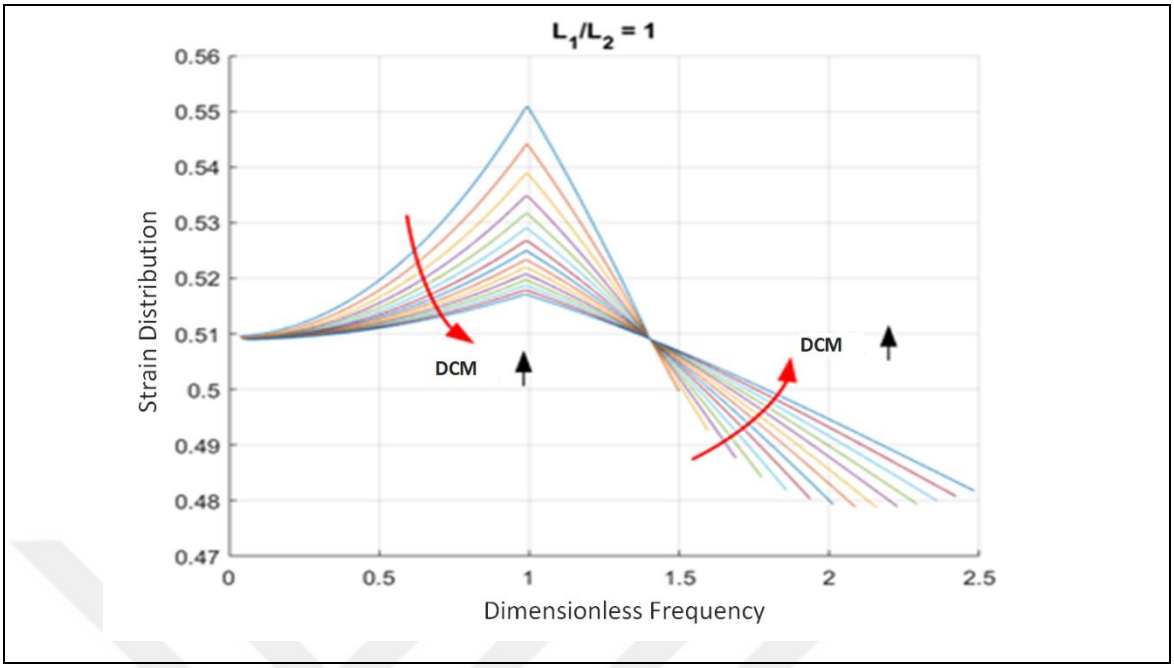

Figure 5.11. Strain distribution when DCM is fine-tuned for $\boldsymbol{L_1/L_2 = 1}$

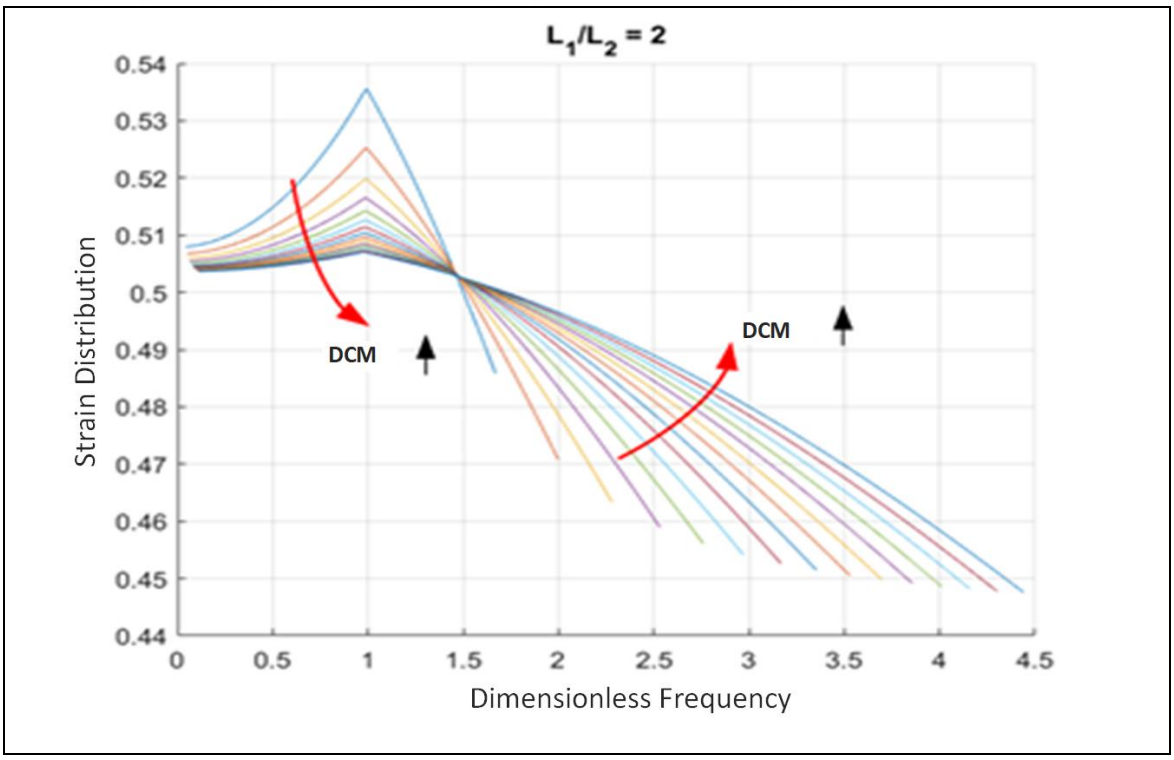

Figure 5.12. Strain distribution when DCM is fine-tuned for $\boldsymbol{L_1/L_2 = 2}$

As can be seen in the figures, increasing the DCM generally improves the strain distribution in the non-resonance region, while decreasing the strain distribution in the resonance region. However, considering that there are many different parameters that affect the system dynamics and that the analytical model is created with many pre-assumptions and simplifications, it is obvious that the most reliable result is a sensitive experimental study.

6. EXPERIMENTAL VERIFICATION

The experimental procedure for measuring the strain distribution is described. Model is assembled, measuring setup is manufactured and experimental results are obtained.

6.1. EXPERIMENTAL SETUP

There are some solid models used in the production of the model mechanisms and the measurement setup and some photographs taken during the production.

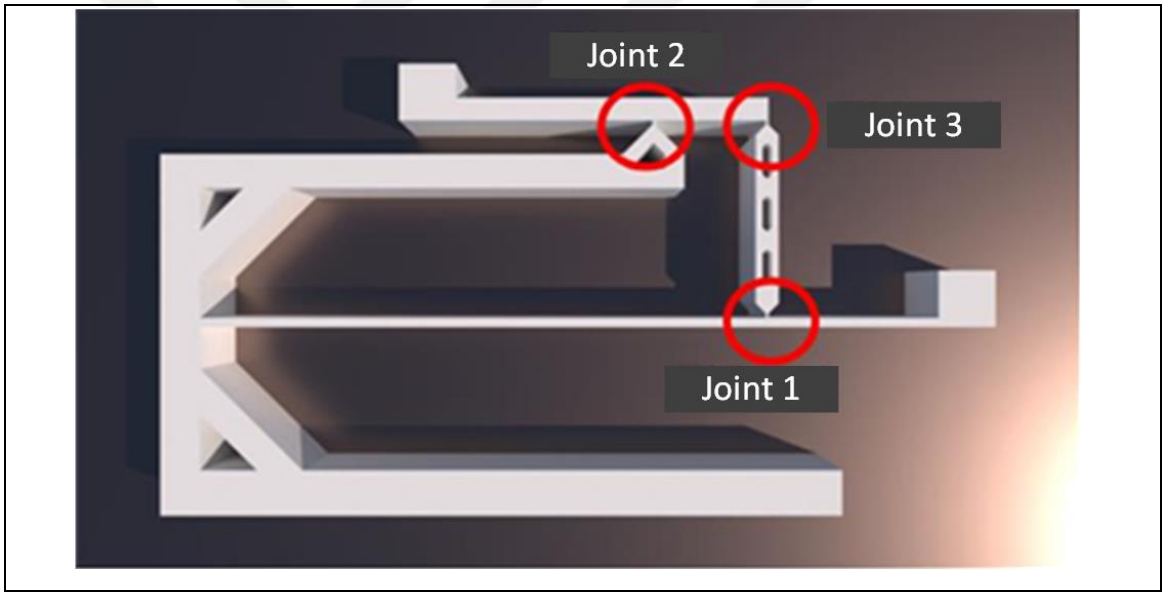

Figure 6.1. Concept design image and joint locations for the model

Figure 6.2. Preliminary prototype for model flexible mechanism approach

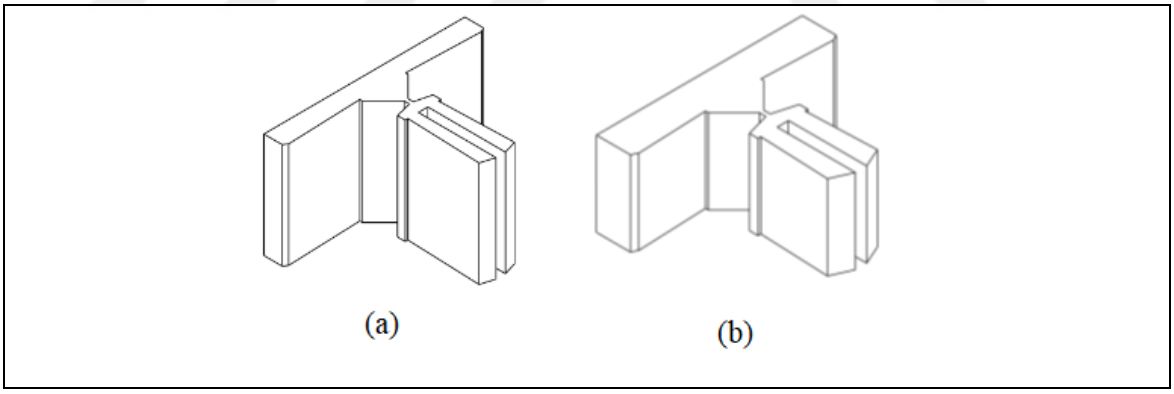

Figure 6.3. Joint 1 for model solid model. (a) Initial state and (b) Last state.

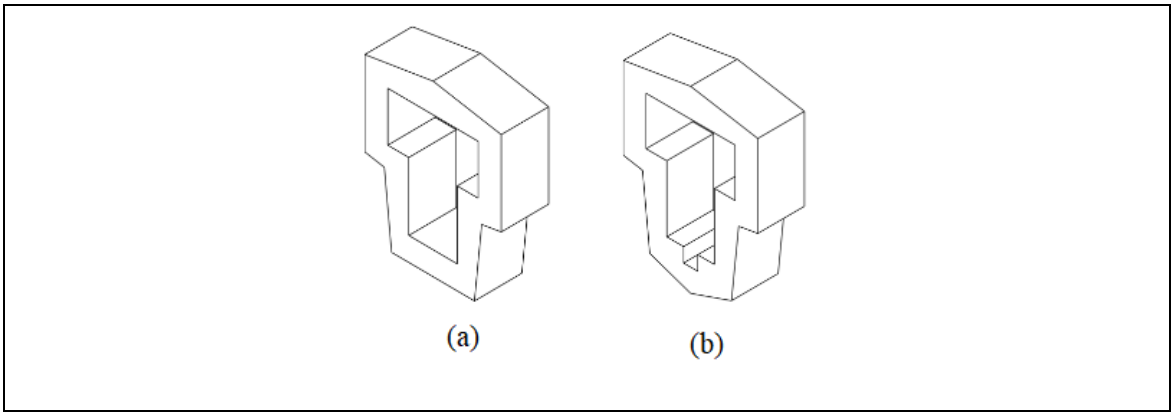

Figure 6.4. Solid model of the state of the shrink-fit frame for the model.

(a) First model and (b) Last model.

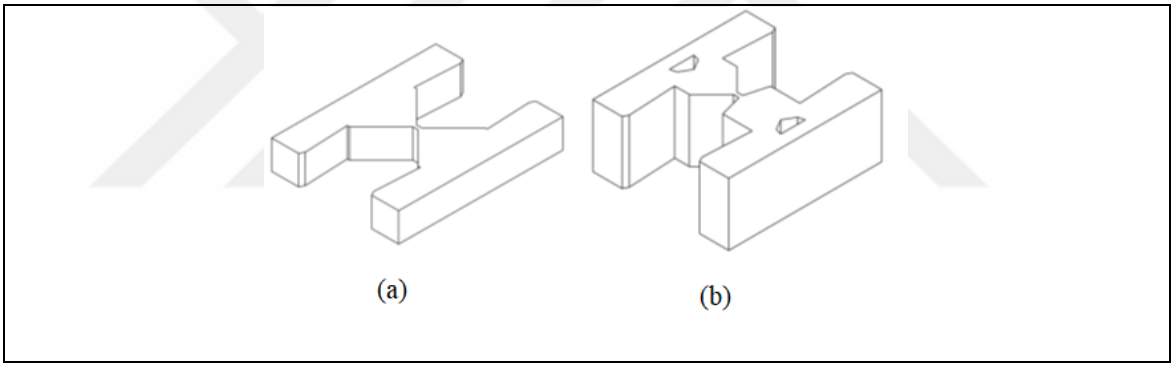

Figure 6.5. Joint 2 solid model. (a) Initial state and (b) Last state.

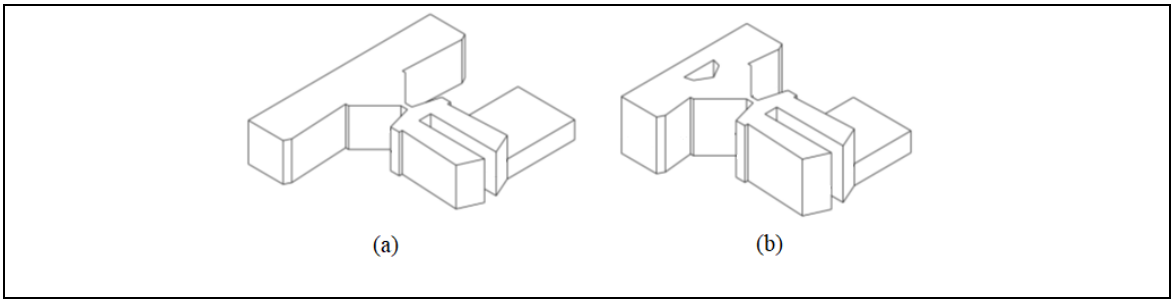

Figure 6.6. Joint 3 solid model. (a) Initial state and (b) Last state.

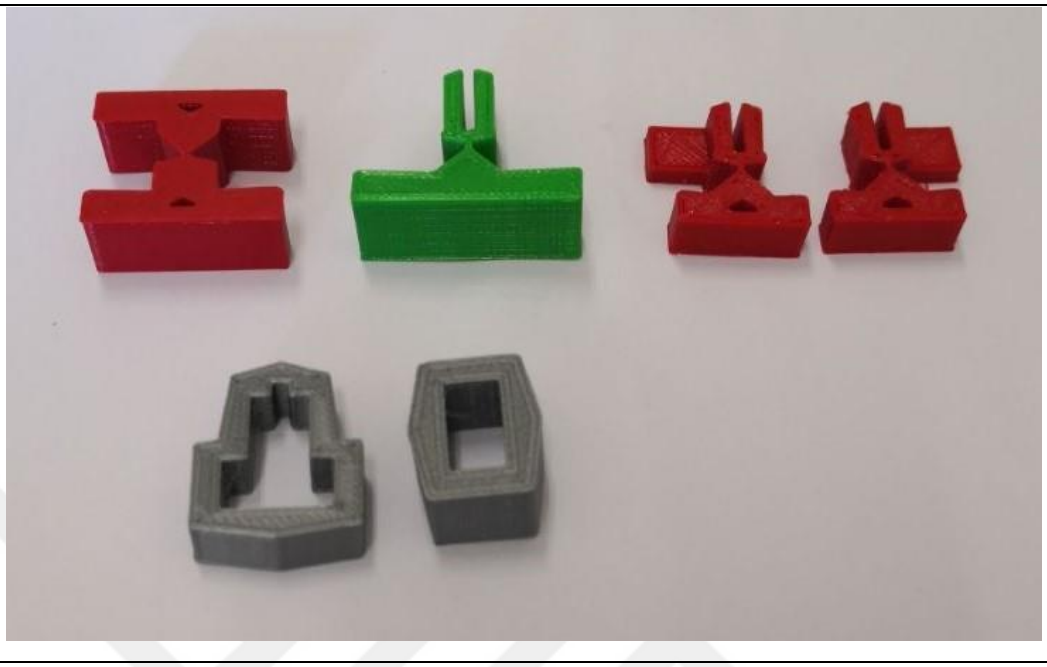

Figure 6.7. Joints and frames for the model

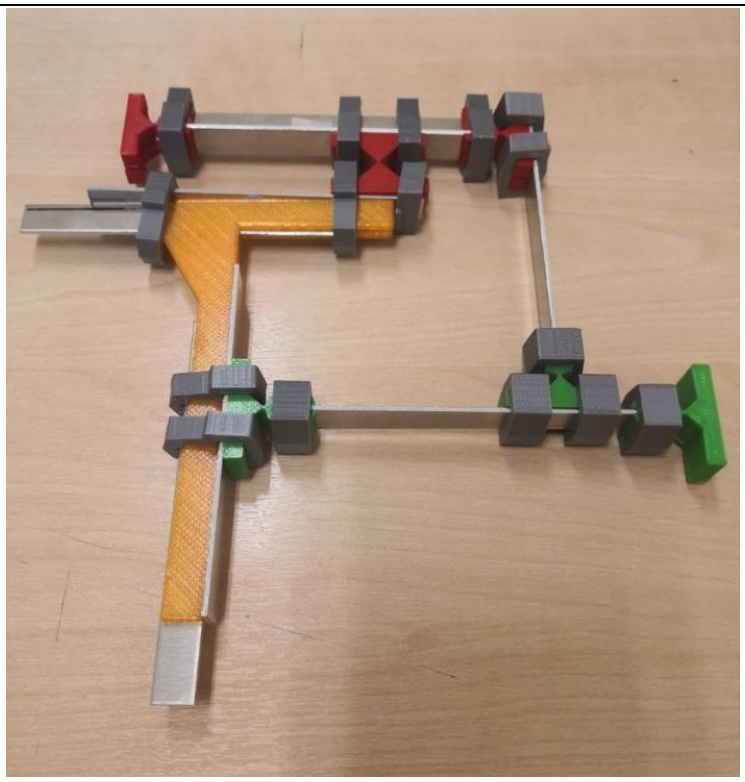

Figure 6.8. Model prototype created for testing joints

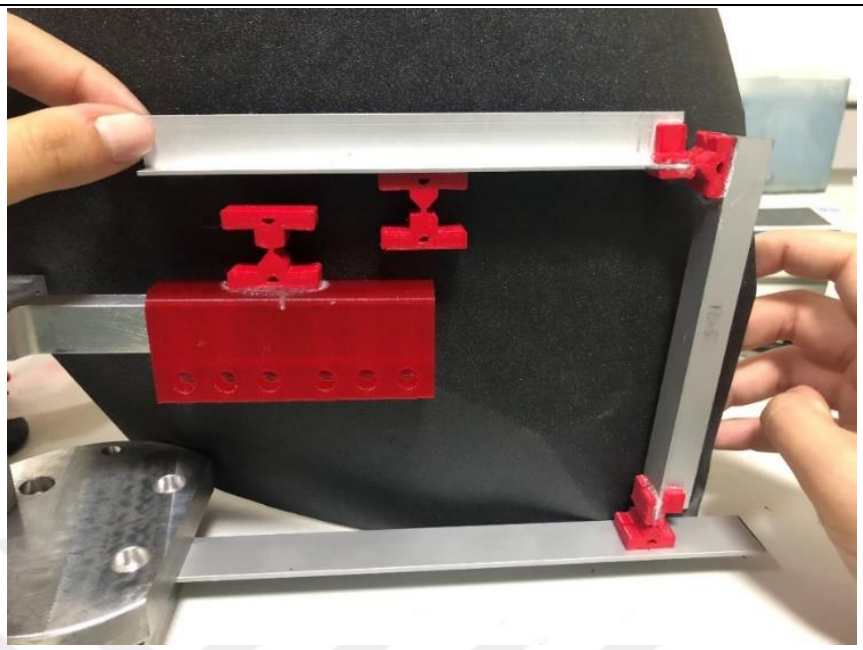

Figure 6.9. Model assembly

Figure 6.10. Image of the manufactured version of the beam holder designed for the model

6.2. MEASUREMENT SETUP

A mechanism is designed and the general skeletal structure of the linear working mechanism is preserved.

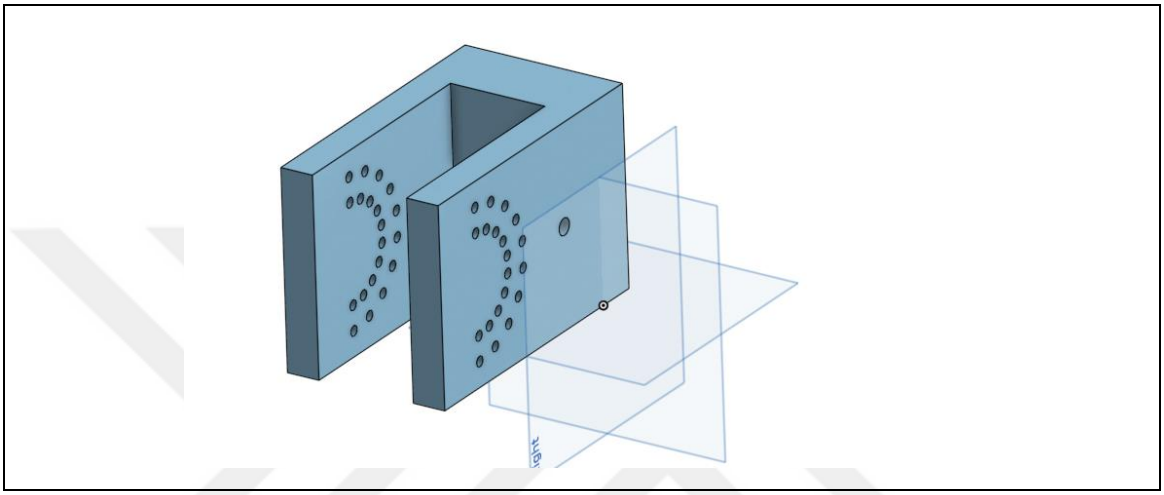

Figure 6.11. Isometric view of the solid model of the part that changes the height and angle

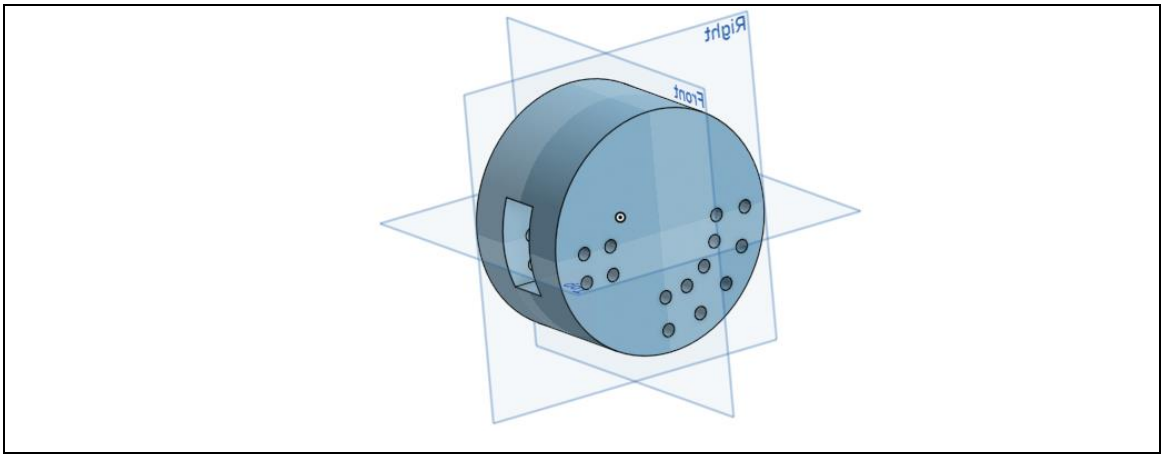

Figure 6.12. Solid model of the part that changes the angle

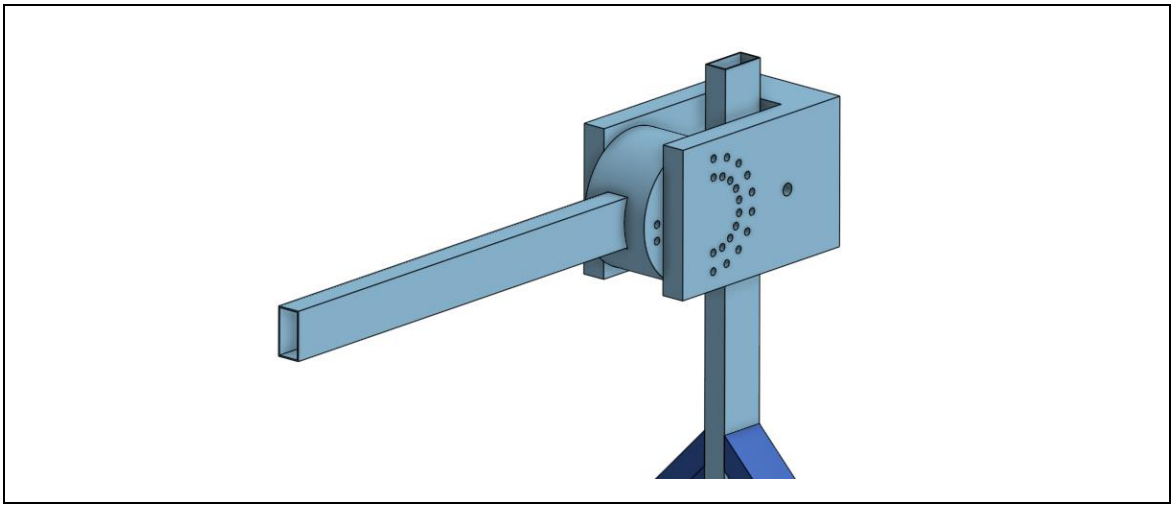

Figure 6.13. Isometric view of the assembled solid model of the linear transport assembly

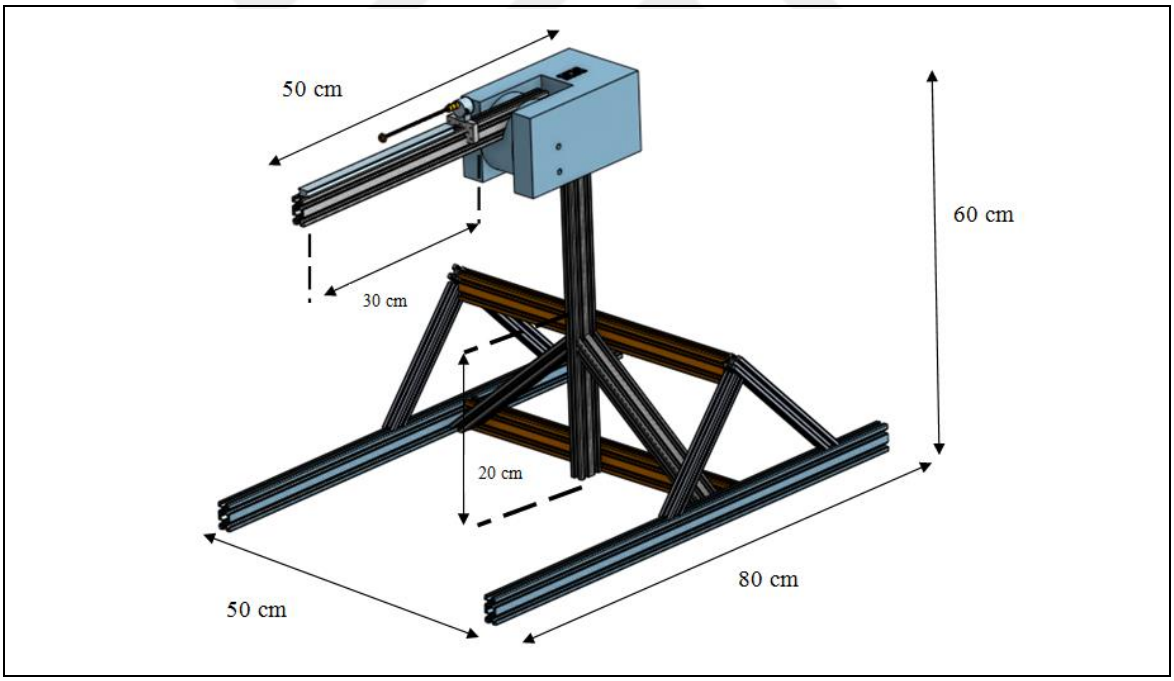

Figure 6.14. Isometric view of the final measuring setup

SICK OD5 brand laser displacement sensor in the measurement setup can accurately read the displacement data without contact and sample with high frequency. The laser displacement sensor can be moved linearly at a constant speed on a line with the help of a

ball screw, stepper motor and controller. The deflection function of the beam can be obtained by the movement of the sensor from the base to the end of the beam under vibration. Schematic view of the mechanism is given in Figure 6.15.

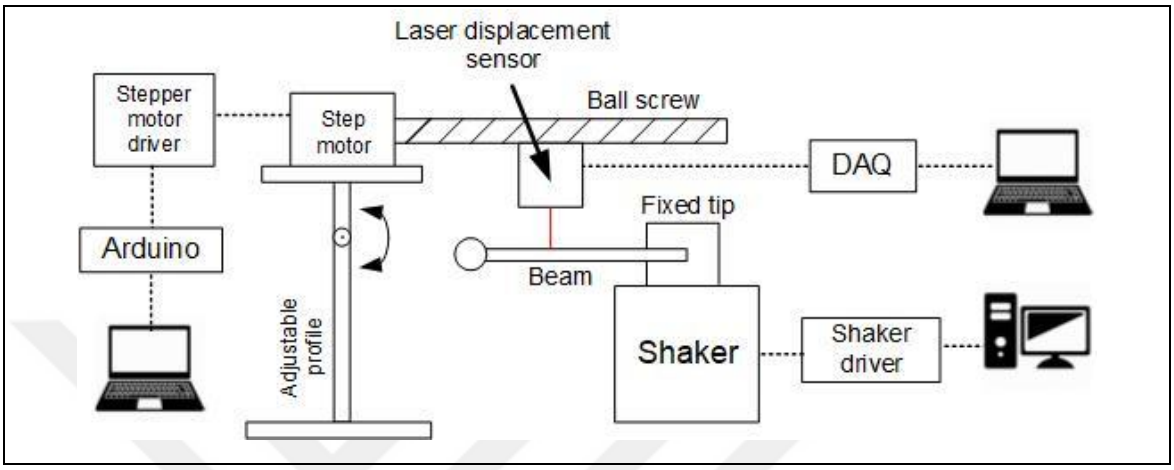

Figure 6.15. Schematic representation of the experimental setup

Experimental procedure flow diagram is given in Figure 6.16. After the beam mechanism produced is connected to the shaker and the measurement device with laser displacement sensor is positioned appropriately, the frequency sweep test is performed first, and the frequency response of the relative position of the end point of the beam relative to the root, namely the deflection, is obtained and the resonance frequency is determined from there. Then, vibration data is obtained with the measurement setup by producing a fixed frequency vibration at frequency values determined according to the resonance frequency. In this way, raw data is obtained.

A series of procedures are required to obtain the deflection curve of the beam from the raw data obtained. First, a bandpass filter is applied to the data in order to prevent high frequency noise and movements caused by the vibration of the low frequency environment. Although the signal obtained is cleaner, in order to find the deflection function of the beam, it is necessary to subtract the fundamental shake produced by the shaker from this signal. Another purpose of this process is to verify that the measurement made is accurately. The harmonic displacement observed at the root of the beam is extended synthetically along the beam and extracted from the beam displacement raw data. This process is shown in Figure 6.17. Here, the purple colored part shows the fundamental shake and the light blue signal

shows the vibration data from which the fundamental shake is extracted. The extracted basic shake is shown in blue. Here, it is seen that both the signal in the raw data and the synthetically produced fundamental jolt coincide with the sinus peaks. This shows that the laser displacement sensor moves at a constant speed from the root to the tip and the vibration frequency remains constant during the measurement. This result showed the reliability of the measurement.

Deflection curve was obtained by combining the peak values of the filtered signal and by fitting a fifth-degree polynomial to this curve, the deflection curve could be mathematically expressed depending on the axial position on the beam. In order to find the strain, the second derivative of the deflection curve with respect to the position must be taken. After polynomial fitting, the second derivative of the polynomial with respect to position is simply taken, so the strain with respect to the axial position is found. The strain distribution is obtained by taking the average of the obtained strain data and dividing it by the maximum strain value.

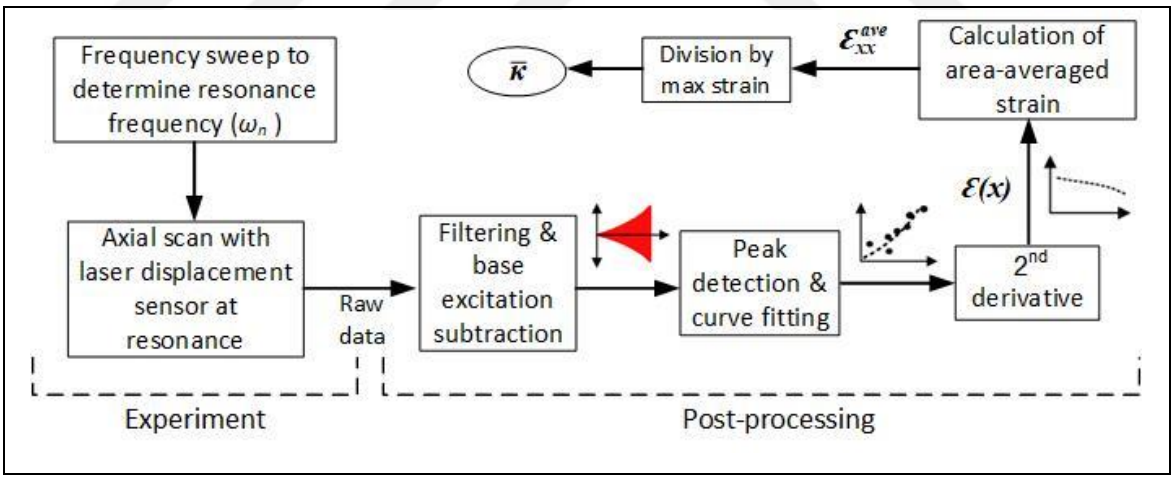

Figure 6.16. Experimental procedure flow diagram

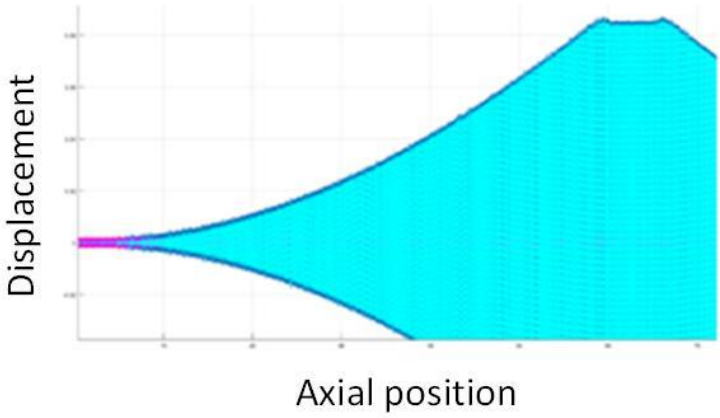

Figure 6.17. Subtracting foundation shake from beam displacement data

6.3. EXPERIMENTAL RESULTS

The strain distribution on the flexible beam has been measured experimentally. The general schematic view of model is given in Figure 2.1. The version of the mechanism connected to the shaker is given in Figure 6.18. The fixed parameters of the system are given in Table 6.1.

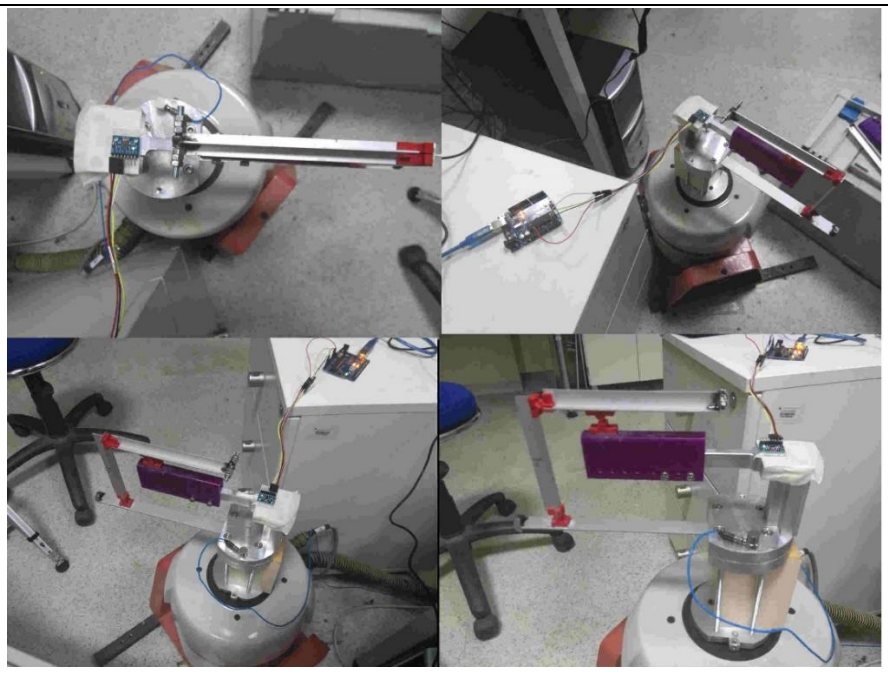

Figure 6.18. Photograph of Model assembly attached to the shaker

Table 6.1. Fixed parameters

Flexible beam's length	200 mm
Flexible beam's width	20 mm
Flexible beam's thickness	2 mm
Connecting beam' s length	154 mm
Tip mass	10 g
ε ratio (Figure 2.1)	0.8

The effects of two different parameters on the strain distribution is investigated. The first of these is the leverage ratio (L_1/L_2) , the other is the dimensionless counter-mass (M'/M) . Also, the frequency response of the strain distribution is found by changing the dimensionless frequency (ω/ω_1) parameter.(ω: force frequency, ω_1: fundamental natural frequency). Dimensionless counter mass is the ratio of the total weight of the bolt and nut used as the counter mass to the total weight of the elastic beam.

An example of using bolts and nuts as opposing mass is Figure 6.19

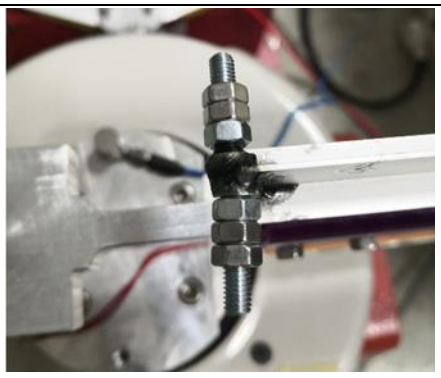

Figure 6.19. Bolts and nuts forming the opposing mass

Before measuring the strain distribution, the frequency response of the beam end displacement for different counters of mass is found. Thus, both the system's functioning as a resonator is tested and the effect of the opposing mass on the resonance frequency and frequency response is observed. The result of this experiment in which the leverage ratio is two is given in Figure 6.20 graphically. There are two from each curve, which are increasing

frequency (up-sweep) and decreasing frequency (down-sweep). As can be seen, the resonance frequency also decreases with the increase of $\mathbf{M'/M}$ ratio (Figure 6.20).

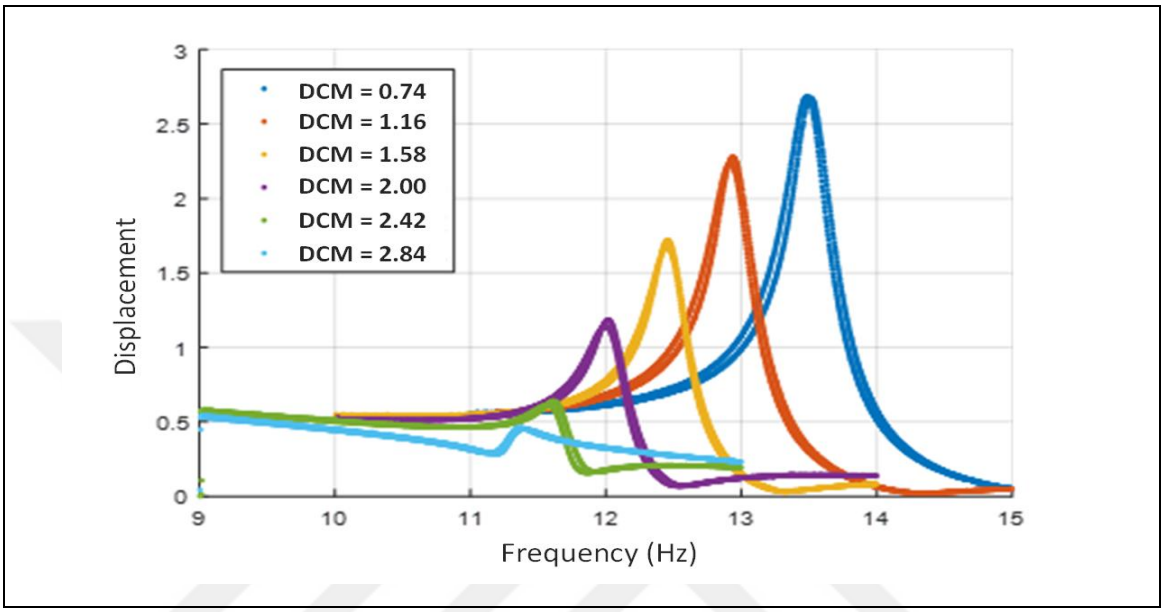

Figure 6.20. Frequency response of beam tip displacement

First of all, it is tested for the case where the leverage ratio is equal to one. The results of the experiment are given in Figure 6.21. Here the graph on the left shows the strain distribution for different dimensionless counter mass values. Each symbol corresponds to a dimensionless counter-mass value. For example, the blue circle represents the case where the dimensionless counter-mass is 1.58. The reason there are more than one blue circle is because each coincides with a different dimensionless frequency. For this reason, for example, for the frequency response where the dimensionless counter-mass is 1.58, the blue circle values should be looked at in the graph on the right. Thus, for any dimensionless counter mass, both the frequency response can be seen on the right graph, and it is possible to compare it with the other dimensionless counter masses with the graph on the left.

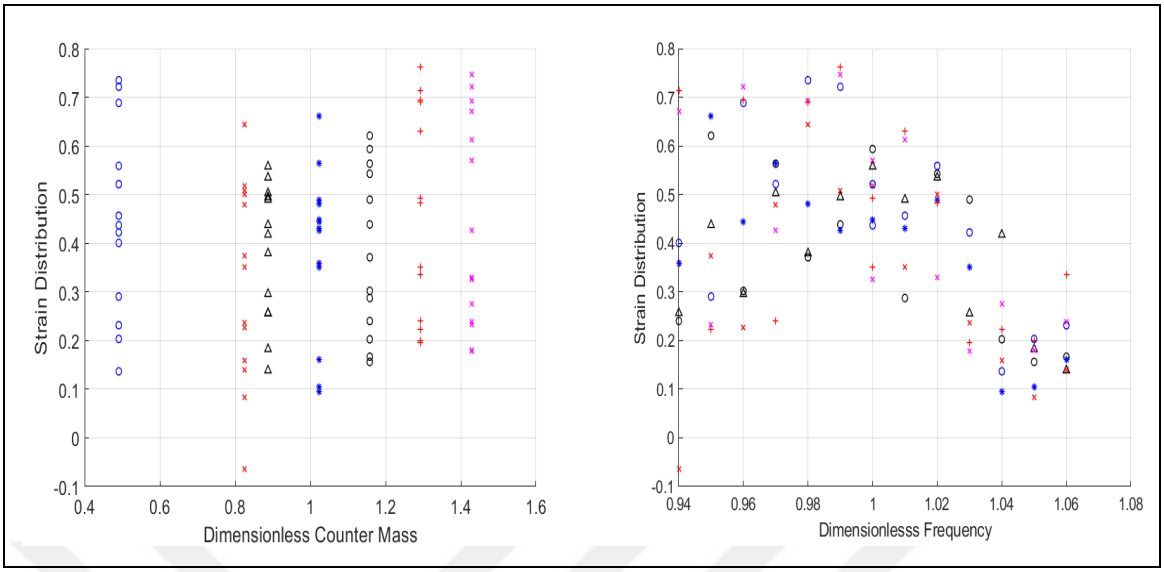

Figure 6.21. Strain distribution ($L_1/L_2 = 1$)

As a result of the experiment, it is seen that the strain distribution frequency response generally peaks in the resonance region and decreases in the regions other than resonance. But above the resonance, ie the part where the dimensionless frequency is greater than one, the decrease is greater. When the strain distribution values are examined, it is seen that the strain distribution exceeds 0.7 for many dimensionless counter mass values. After the promising results seen in Figure 6.21, the mechanism is produced using different leverage ratios and new experiments are made. The results of the experimental study for the ratio $L_1/L_2 = 0.5$ are given in Figure 6.22. Similar to the case of $L_1/L_2 = 1$, a situation occurred in which the strain quickly loses its homogeneity on the resonance. Again, it is seen that the strain distribution reaches 0.7 levels. However, it is determined that when the dimensionless counter mass is 3.28, the strain distribution is at 0.57, that is, well below the standard rectangular beam.

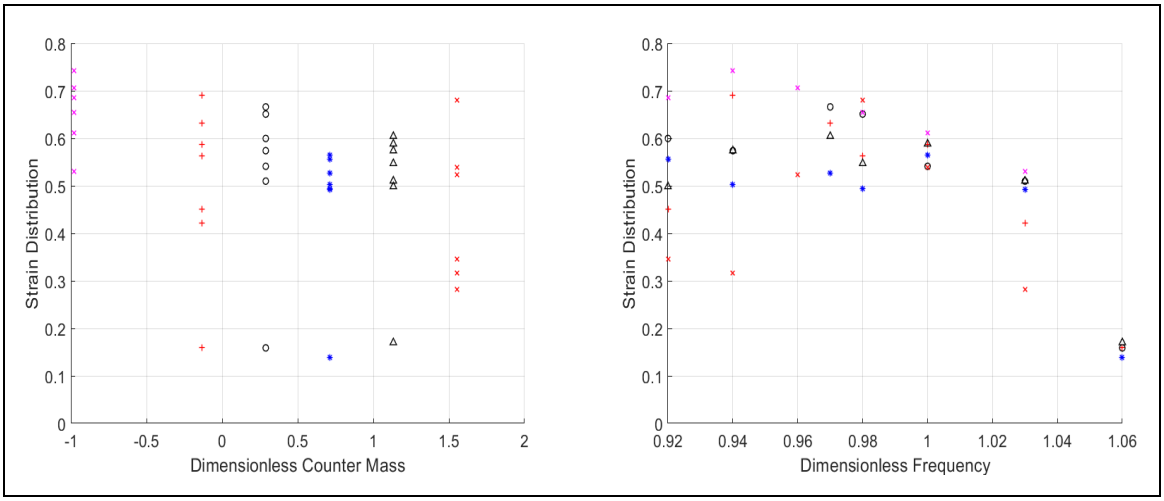

Figure 6.22. Strain distribution ($L_1/L_2 = 0.5$)

It will not be possible to obtain the desired homogeneous strain distribution if the leverage ratio cannot produce sufficient counter force against the elastic beam tip mass. For this reason, it is decided to increase the leverage ratio and the strain distribution tests are performed for the ratio($L_1/L_2 = 2$). Results are given in Figure 6.23. Unlike the previous two experiments, high strain distribution is obtained here over a wider non-dimensional counter-mass range. In addition, when the frequency response of the strain distribution is examined, again a high strain distribution is obtained before and in the resonance region.

Although the findings obtained for the ratio $L_1/L_2 = 2$ show that this configuration may be suitable for the energy generator, an experimental study has been carried out for the ratio $L_1/L_2 = 4$ in order to see the behavior of the system at a higher leverage ratio. As can be seen from the results given in Figure 6.24, the strain distributions are quite low compared to the results obtained in the case of $L_1/L_2 = 2$. The only high strain distribution is when no bolts and nuts are put at the end of the lever beam, i.e. the counter mass is zero. In this case, the moment created by the weight of the lever beam itself constitutes the counter force and a high strain distribution can be obtained. However, when the counter mass is increased, the strain distribution starts to decrease again.

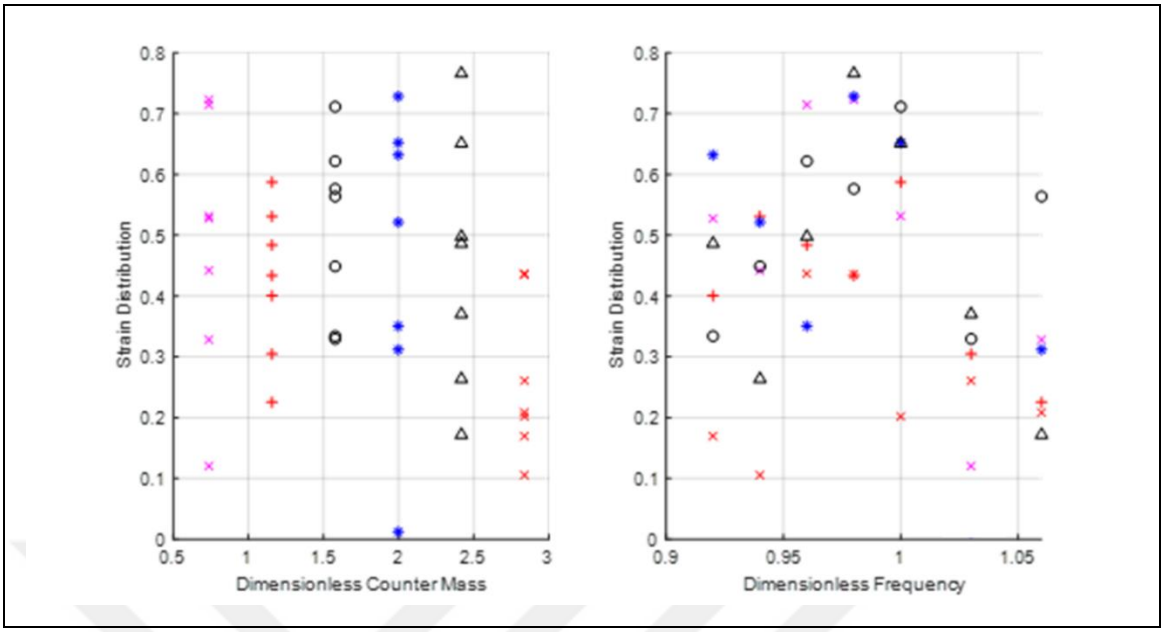

Figure 6.23. Strain distribution ($L_1/L_2 = 2$)

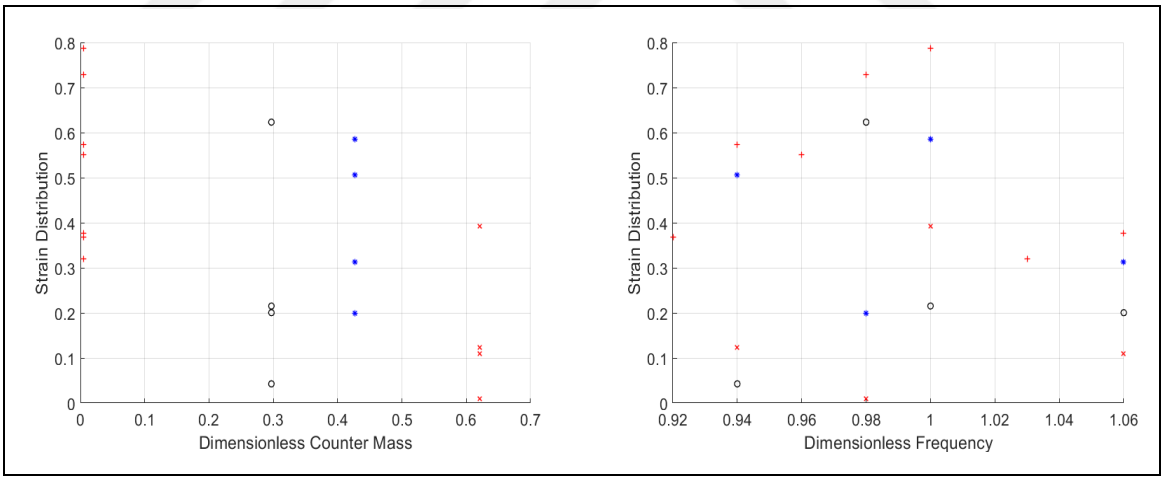

Figure 6.24. Strain distribution ($L_1/L_2 = 4$)

6.3.1. Differences of Experimental and Analytical Model

In the analytical model, lever and connecting beams are very high elastic modulus and very low density, but in experimental method, t-cross section aluminium is chosen for the Lever and connecting beam. While hinges are produced with a 3D printer and material is polyurethane in experimental setup, in analytical model lever effect of hinges are neglected. Besides, tip and counter masses are not point mass in experimental model, but so in the analytical model. Therefore, it is not expected to be an experimental model with analytical model and finite element. The aim is to show that it has a better strain distribution than the conventional cantilever beam. At the same time, it is aimed to show that the strain distribution can be increased by adjusting DCM.

7. CONCLUSION

Cantilever beam type vibration energy harvester with a lever mechanism and a counter mass are modelled as analytically and numerically (FEM).The objective is to increase energy conversion efficiency by obtaining a more uniform stress distribution within the piezoelectric cantilever beam. A analytical model is constructed using the Euler-Bernoulli beam theory. Although, FEM results and analytical model results are very close in natural frequency, in harmonic analysis it is seen that when the leverage ratio is increased, difference between the finite element model and the analytical model is increased. Since, finite element model is made using shell elements and includes high deformation. In the analytical model, Euler-Bernoulli beam theory is used and it is accepted that the beam deformations are small. In addition, it is assumed that the connecting beam is always vertical and does not transmit horizontal force to the harmonic beam. It is assumed that the angle β formed by the horizontal beam of the lever beam during vibration is small and small angle approach is made while writing the equation of motion. The effects of counter mass and leverage ratio are seen on stress uniformity within the excitation frequency. Since, the strain distribution in a piezoelectric beam with a static transverse load at the end is that the average strain is half the maximum strain approximately (0.5). In the model it is seen that by changing the design parameters, the strain distribution increases above 0.53 (Figure 5.9) . In the test results, When the strain distribution results are examined, high strain distribution has been obtained in many configurations. It is seen that the strain distribution around the resonance is high. It gives high strain values on average ±2-3 percent of the resonance frequency. The stress distribution is above 0.7 in all four models at certain DCM. When leverage ratio is 0.5, 1, 2, 4 strain distibution is seen as respectively 0.75 (Figure 6.22), 0.76 (Figure 6.21), 0.77 (Figure 6.23), 0.78 (Figure 6.24). As a result of this study It is shown that DCM by changing the DCM and leverage ratio values, stress uniformity can be improved compared to a conventional cantilever beam energy harvester.

Improving the finite element model: Although adding a piezoelectric material layer to the finite element beam model is one of the improvements that can be made.

Joint modeling: By creating an experimental setup, the spring constant and damping ratios of the rotary and prismatic joints pressed with flexible thermoplastic materials by additive

manufacturing methods can be found. If this situation is added to the mathematical model, it will be possible to obtain more realistic mathematical models.

There are problems that may occur with the use of experimental model in a commercial product: Experimental model has difficulty aligning and adhering to hinges, tip and counter masses. Life cycle is shorter to generate energy than conventional cantilever beam. Maintenance is more difficult.

REFERENCES

1. Shaikh FK, Zeadally S. Energy harvesting in wireless sensor networks: A comprehensive review. *Renewable and Sustainable Energy Reviews.* 2016;55(1):1041-1054.
2. Starner T. Human-powered wearable computing. *IBM Systems Journal.* 1996;35(3,4):618-629.
3. Xie L, Du R. Frequency tuning of a nonlinear electromagnetic energy harvester. *Journal of Vibration and Acoustics*. 2013;136(1):011010-011010-7.
4. Naruse Y, Matsubara N, Mabuchi K, Izumi M, Honma K. Electrostatic micro power generator from low frequency vibration such as human motion. *Journal of Micromechanics and Microengineering.* 2009;19(9):19-22.
5. Wang Xu, Lin L. Dimensionless optimization of piezoelectric vibration energy harvesters with different interface circuit. *Smart Materials and Structures.* 2013;22(8):85011-20.
6. Wickenheiser A. Analysis of energy harvesting using frequency up-conversion by analytic approximations. *Small-Scale Energy Harvesting.* 2012;9(1):211-234.
7. Roundy S, Leland ES, Baker J, et al. Improving power output for vibration-based energy scavengers. *IEEE Pervasive Computing.* 2005;4(1):28-36.
8. Kong L, Zhang J, Wang H, et al. Simulation study of MEMS piezoelectric vibration energy harvester based on c-axis tilted AlN thin film for performance improvement. *AIP Advances.* 2016;6(12):125128-12.
9. Reddy AR, Umapathy M, Ezhilarasi D, Uma G. Cantilever beam with trapezoidal cavity for improved energy harvesting. *International Journal of Precision Engineering and Manufacturing.* 2015;16(8):1875-1881.
10. Raju S.S, Umapathy M, Uma G. Cantilever piezoelectric energy harvester with multiple cavities. *Smart Mater Struct.* 2015;24(11):115023.
11. Ma X, Wilson A, Rahn CD, Trolier-McKinstry S. Efficient energy harvesting using piezoelectric compliant mechanisms: theory and experiment. *Journal of Vibration and Acoustics.* 2016;138(2):21005.

12. Yoon HS. Modeling, optimization, and design of efficient initially curved piezoceramic unimorphs for energy harvesting applications. *Journal of Intelligent Material Systems and Structures*. 2015;16(10):877-888.

13. Xie X, Livermore C. A high-force, out-of-plane actuator with a MEMS-enabled microscissor motion amplifier. *Journal of Physics, Conference Series*. 2015;660(15):12026.

14. Halvorsen E, Dong T. Analysis of tapered beam piezoelectric energy harvesters. *Proceedings of PowerMEMS.* 2008:241-244.

15. Rosa M, De Marqui Junior C. Modeling and analysis of a piezoelectric energy harvester with varying cross-sectional area. *Shock and Vibration.* 2014;2014(1):930503-9

16. Xiong X, Olutunde Oyadiji S. Tapered two-layer broadband vibration energy harvesters. *Journal of Vibration and Acoustics*. 2015;137(3):31011-31014.

17. Meirovitch L. *Fundamentals of vibrations*, McGraw-Hill; 2001.

18. Erturk A, Inman DJ. On mechanical modeling of cantilevered piezoelectric vibration energy harvesters. *Journal of Intelligent Material Systems and Structures*. 2015;19(11):1311-1325.

19. Kianpoor A, Jahani K. Modeling and analyzing of energy harvesting fromtrapezoidal piezoelectric beams. *Iranian Journal of Science and Technology*. 2015;43(1):259-266.

20. Hosseini R, Nouri M. Shape design optimization of unimorph piezoelectriccantilever energy harvester. *Journal of Computational Applied Mechanics.* 2016;47(2):247-259.

21. Wang L, Tong X, Yang H, Wei Y, Miao Y. Design and analysis of a hollow triangular piezoelectric cantilever beam harvester for vibration energy collection. *International Journal of Pavement Research and Technology*. 2019;12(3):259-268.

22. Izadgoshasb I, Lim YY, Padilla RV, Sedighi M. Performance enhancement of a multiresonant piezoelectric energy harvester for low frequency vibrations. *Energies*. 2019;12(14):2770-16

23. Inman DJ. *Engineering vibration.* Englewood Cliffs, NJ: Prentice Hall; 1994.

24. Karadag CV, Ertarla S, Topaloglu N, Okyar AF. Optimization of beam profiles for improved piezoelectric energy harvesting efficiency. *Structrural and Multidisciplinary Optimization.* 2020;158(20):0271

APPENDIX A: CODES

Algorithm A.1. FEM code of modal analysis

```
% MATLAB
% GEOMETRY PARAMETERS:

L = 0.1;                                %length of the beam in m

width = 0.02;                           %width of the beam in m

thck = 0.002;                           %thichness of the beam in m


% DENSITY and YOUNGS MODULUS

E = 69e9;                               %Elastic modulus of the beam in GPa

rho = 2700;                             %Density in kg/m^3


%FORCE

F=20;                                   %N


% INPUT EXCITATION PARAMETERS:

w = 400;                                %Excitation freq. in rad/s

N = 5; % Number of mode shapes


% DERIVED PARAMETERS

A = thck*width;                         % Cross sectional area
```

Algorithm A.1. Continued

```
I = (1/12)*width*thck^3;                    %Moment of inertia

c = sqrt(E*I/(rho*A));

betaL = zeros(N,1);

x_array = linspace(0,L,200);



% MODAL ANALYSIS RESULT (UNDAMPED):

betaL(1) = 1.87510407;

betaL(2) = 4.69409113;

betaL(3) = 7.85475744;

betaL(4) = 10.99554073;

betaL(5) = 14.13716839;



if N>5

   for i = (6:1:N)

      betaL(i) = (2*i-1)*pi/(2*L) ;

   end

end

beta = betaL./L;



wr=beta.^2*c; % Creating the natural frequency vector
```

Algorithm A.1. Continued

```
for i = 1:1:N

   zeta(i) = (sin(betaL(i))-sinh(betaL(i)))/(cos(betaL(i))+cosh(betaL(i)));

   mode_shape_fun = @(x)(cos(beta(i)*x)-cosh(beta(i)*x) +zeta(i)*(sin(beta(i)*x)-sinh(beta(i)*x)));

   mode_shape_sq_fun = @(x)(cos(beta(i)*x)-cosh(beta(i)*x) +zeta(i)*(sin(beta(i)*x)-sinh(beta(i)*x))).^2;

   Lambda(i) = integral(mode_shape_fun,0,L);

   Psi(i)= integral(mode_shape_sq_fun,0,L);

   for j = 1:length(x_array)

      xx = x_array(j);

      modal_magn(i,j) = (cos(beta(i)*xx)-cosh(beta(i)*xx) + zeta(i)*(sin(beta(i)*xx)-sinh(beta(i)*xx)));

  square_phi= modal_magn(i,j)^2;

   end

end

 y=(square_phi.*F)./(Psi.*(wr.^2-w^2).*(rho.*A));

max(y(:))
```

Algorithm A.1. Continued

```
! Modal Analysis FEAP Finite Element Model

feap **

0   0   0   3   6   4



PARA

 mt    = 0.01      !tip mass

 me    = 0.5       !!M/M' ratio

 mc    = me*mt     !counter mass

 Le    = 1         !Lever ratio

 L2    = 154/(Le+1)  !L2

 L1    =154-L2       !L1

 L     = 200     !elastic beam length

 ep    = 0.8      !epsilon ratio

 wt    = 20       !beam width

 hy    = 70       !connecting beam length

 Li    = L*ep-L1-L2  !initial position of the lever beam in the x direction

 bx    = 120      !Number of elastic beam elements in x direction

 by    = 8        !Number of elastic beam elements in y direction

 cy    = 8        ! Number of connecting beam elements in the y direction

 cz    = 14       ! Number of connecting beam elements in the z direction

 lx    = L1+L2    !Number of lever beam elements in the x direction
```

Algorithm A.1. Continued

```
 ly   = 8        !Number of lever beam elements in the y direction

 ln = (bx+1)*(by+1)+(cy+1)*(cz+1)+L1+1  !Lever beam L1 end node no

 lm = (bx+1)*(by+1)+(cy+1)*(cz+1) !Total element of elastic and connecting beams

 cm = (bx+1)*(by+1)+(cy+1)*cz+1  !Connecting beam top point first node

 bl =  ep*bx+1 !First node in the elastic beam connecting beam connection

 cl =  lm+lx+1 !First node in the lever beam connecting beam connection

 bt = (bx+1)*(by+1) !Elastic beam total number of nodes

 bm =  (by+1+1)/2  !Elastic beam tip mass connection midpoint


% material 1: elastic beam

MATE  1

SHELL

 ELAStic, ISOTropic,  69.0e+6  .330e-0 !Eleastic module ve Poisson ratio

 THIC,     , 2 !thickness

 DENS,      ,2.7e-6 ! density


% material 2: connecting beam

MATE  2

 SHELL

 ELAStic, ISOTropic,  210e+10  .290e-0

 THIC,     , 2
```

Algorithm A.1. Continued

```
DENS,      ,7.8e-9

% material 3: lever beam

MATE  3

 SHELL ELAStic, ISOTropic,  210e+10  .290e-0

 THIC,     , 2

 DENS,      ,7.8e-9



! Creating geometries

BLOC ! Elastic beam

 CART bx by

  QUAD 4

  MATE 1

   1 0  0 0

   2 L  0 0

   3 L  0 wt

   4 0  0 wt



BLOC ! Connecting beam

 CART cy cz

  QUAD 4

  MATE 2
```

Algorithm A.1. Continued

```
 1 Li+L1+L2 0  0

 2 Li+L1+L2 0  wt

 3 Li+L1+L2 hy wt

 4 Li+L1+L2 hy 0


BLOC ! lever beam

 CART lx ly

 QUAD 4

 MATE 3

  1  Li       hy 0

  2  Li+L1+L2 hy 0

  3  Li+L1+L2 hy wt

  4  Li       hy wt


BOUN ! Elastic beam cantilever support boundary conditions

 1          bx+1 -1 -1  0 -1 -1 -1

 by*(bx+1)+1  0   1  1  1  1  1  1


BOUN ! Lever beam support point boundary conditions

 ln           lx+1  -1 -1 0 -1 -1 0

 ln+(lx+1)*(ly) 0     1  1 1  1  1 0
```

Algorithm A.1. Continued

```
MASS ! Assignment of tip and counter mass
 (bx+1)*(bm)      0 mt mt mt 0 0 0    even
 lm+1+(lx+1)*ly/2 0 mc mc mc 0 0 0
END


LINK ! Rotational joint connections
 bl              bt+1  bx+1  1 0 0 0 0 1 1
!link1: Between elastic beam connecting beam
 bl+(bx+1)*by     bt+cy+1 0   0 0 0 0 0 1 1
 cl               cm  lx+1 1 0 0 0 0 1 1


!link2: Between connecting beam lever beam
 lm+(ly+1)*(lx+1)    lm   0   0 0 0 0 0 1 1
batch
end


batch
 plot mesh
 plot boun
end
batch ! Modal analysis
```

Algorithm A.1. Continued

```
 MASS

 TANG

 SUBS,,3

 EIGV ALL,,1

END

INTE

STOP
```

Algorithm A.2. Harmonic response Analysis FEAP finite element model

```
! Metot 2 – Harmonic Response Analysis FEAP Finite Element Model

*COMPLEX

feap **

0   0   0   3   6   4



PARA

 mt    = 0.01      !Tip mass

 me    = 0.5       !!M/M' ratio

 mc    = me*mt     !Counter mass

 Le    = 1         !Lever ratio

 L2    = 154/(Le+1)  !L2

 L1    =154-L2      !L1

 L     = 200       !Elastic beam length

 ep    = 0.8       !Epsilon ratio

 wt    = 20        !beam width

 hy    = 70        ! connecting beam length

 Li    = L*ep-L1-L2 !initial position of the lever beam in the x direction

 bx    = 120       !Number of elastic beam elements in x direction

 by    = 8         !Number of elastic beam elements in y direction

 cy    = 8         ! Number of connecting beam elements in the y direction

 cz    = 14        ! Number of connecting beam elements in the z direction
```

Algorithm A.2. Continued

```
 lx   = L1+L2    !Number of lever beam elements in the x direction

 ly   = 8        !Number of lever beam elements in the y direction

 ln = (bx+1)*(by+1)+(cy+1)*(cz+1)+L1+1  !Lever beam L1 end node no

 lm = (bx+1)*(by+1)+(cy+1)*(cz+1) !Total element of elastic and connecting beams

cm = (bx+1)*(by+1)+(cy+1)*cz+1  !Connecting beam top point first node

 bl =  ep*bx+1 !First node in the elastic beam connecting beam connection

 cl =  lm+lx+1 !First node in the lever beam connecting beam connection

 bt = (bx+1)*(by+1) !Elastic beam total number of nodes

 bm =  (by+1+1)/2  ! Elastic beam tip mass connection midpoint

 et =  0.01 ! Damping ratio

 y  =  1   ! Base excitation amplitude


% material 1: elastic beam

MATE  1

SHELL

 ELAStic, ISOTropic,  69.0e+6  .330e-0 !Elastic modül ve Poisson ratio

 THIC,     , 2 !thickness

 DENS,      ,2.7e-6 ! density


% material 2: connecting beam

MATE  2
```

Algorithm A.2. Continued

```
 SHELL
 ELAStic, ISOTropic,  210e+10  .290e-0
 THIC,     , 2
 DENS,      ,7.8e-9


% material 2: lever beam
MATE  3
 SHELL
 ELAStic, ISOTropic,  210e+10  .290e-0
 THIC,     , 2
 DENS,      ,7.8e-9


! Creating geometries
BLOC ! Elastic beam
 CART bx by
  QUAD 4
  MATE 1
   1 0  0 0
   2 L  0 0
   3 L  0 wt
   4 0  0 wt
```

Algorithm A.2. Continued

```
BLOC ! Connecting beam
 CART cy cz
  QUAD 4
  MATE 2
  1 Li+L1+L2 0  0
  2 Li+L1+L2 0  wt
  3 Li+L1+L2 hy wt
  4 Li+L1+L2 hy 0


BLOC ! Lever beam
 CART lx ly
  QUAD 4
  MATE 3
   1  Li       hy 0
   2  Li+L1+L2 hy 0
   3  Li+L1+L2 hy wt
   4  Li       hy wt


BOUN ! Elastic beam cantilever support boundary conditions
  1         bx+1 -1 -1  0 -1 -1 -1
```

Algorithm A.2. Continued

```
by*(bx+1)+1  0   1  1  1  1  1  1



BOUN ! Boundary conditions applied to the lever beam support point

 ln          lx+1  -1 -1 0 -1 -1 0

 ln+(lx+1)*(ly) 0     1  1 1  1  1 0


DISP ! Base excitation applied to elastic beam cantilever beam

 1          bx+1 0  y 0

 (bx+1)*by+1 0    0  y 0


DISP ! Base excitation applied to the lever beam support point

 ln          lx+1 0 y 0

 ln+(lx+1)*(ly) 0   0 y 0


MASS ! Assignment of tip and counter mass

 (bx+1)*(bm)      0 mt mt mt 0 0 0    even

 lm+1+(lx+1)*ly/2 0 mc mc mc 0 0 0

 END


LINK ! Rotational joint connections
```

Algorithm A.2. Continued

```
 bl              bt+1  bx+1  1 0 0 0 0 1 1

!link1: Between elastic beam connecting beam

  bl+(bx+1)*by     bt+cy+1 0   0 0 0 0 0 1 1

  cl                cm  lx+1 1 0 0 0 0 1 1

!link2: Between connecting beam lever beam

  lm+(ly+1)*(lx+1)    lm   0   0 0 0 0 0 1 1

batch

end



batch

 plot rotate 1 30

 plot rotate 2 30

 plot mesh ! Mesh representation

 plot boun ! Boundary conditions representation

end



batch

param w = 147.29 ! Forced frequency (rad/s)

    CXSOLve,,w,et ! Harmonic solution

     DISP,,605 ! Node 605 (beam end) displacement

END
```

Algorithm A.2. Continued

```
INTE

batch ! Harmonic response visual representation

 plot rotate 1 30

 plot mesh

 plot boun

 plot load

end



INTE

STOP
```

Algorithm A.3. Method 2- reading data from FEAP result file

```
% MATLAB ile Method 2- Reading Data from FEAP Result File


beam_nz = 9; % Number of nodes in y-direction in elastic beam

beam_nx = 121; % Number of nodes in x-direction in elastic beam

beam_np = beam_nz*beam_nx;  % Total number of nodes in elastic beam

file_nm = 'm1_90_158.vtu';% pview file name


[result] = readf_vtu(file_nm);          % Assigning data to result variable


nodes_a = reshape(result{1,2},3,size(result{1,2},2)/3);

% Node location vector

displ_c = reshape(result{5,2},6,size(result{5,2},2)/6);

% Displacement vector for each node

allst_r = reshape(result{6,2},24,size(result{6,2},2)/24);

% Voltage vector for each node


% x, y, z positions of the elastic beam nodes

beam_nd = zeros(beam_nx,beam_nz,3); beam_st = beam_nd;% to clear

beam_nd(:,:,1) = reshape(nodes_a(1,1:beam_np),beam_nx,beam_nz); % p_x

beam_nd(:,:,2) = reshape(nodes_a(2,1:beam_np),beam_nx,beam_nz); % p_y

beam_nd(:,:,3) = reshape(nodes_a(3,1:beam_np),beam_nx,beam_nz); % p_z
```

Algorithm A.3. Continued

```
% Displacement in x, y, z directions for elastic beam

beam_ds(:,:,1) = reshape(displ_c(1,1:beam_np),beam_nx,beam_nz); % s_x

beam_ds(:,:,2) = reshape(displ_c(2,1:beam_np),beam_nx,beam_nz); % s_y

beam_ds(:,:,3) = reshape(displ_c(3,1:beam_np),beam_nx,beam_nz); % s_z



% Axial stress for elastic beam:

% Element number 20 is used in the stress vector:

% Normal stress at bottom

beam_st(:,:,1) = reshape(allst_r(20,1:beam_np),beam_nx,beam_nz);



%vvvvvvvvvvvvvvvvvvvvvvvvvvvvvvvvvvvvvvvvvvvvvvvvvvvvvvvvvvvvvvvvvvvvvvvvvvvv



% Graphing the displacement and stress of the elastic beam in the system:

figure; hold on; grid; set(gca,'CameraPosition',[819,-75,254])

plot3(nodes_a(3,:),nodes_a(1,:),nodes_a(2,:),'r.') % For all nodes

quiver3(nodes_a(3,:),nodes_a(1,:),nodes_a(2,:),...

    displ_c(3,:),displ_c(1,:),displ_c(2,:),1) % For all nodes

pcolor(beam_nd(:,:,3),beam_nd(:,:,1),beam_st(:,:,1)); %Beam stress

xlabel('z'),ylabel('x'),zlabel('y'),

title('plot for all nodes and contour for the beam')
```

Algorithm A.3. Continued

```
%vvvvvvvvvvvvvvvvvvvvvvvvvvvvvvvvvvvvvvvvvvvvvvvvvvvvvvvvvvvvvvvvvvvvvvvvvv
% Avarage strain calculation:
ord_fix = @(x)(x([1,2,4,3])); % Transition from 2D to 1D
beam_ez = beam_nz-1; % Number of elements in y-direction in a elastic beam
beam_ex = beam_nx-1; % Number of elements in the x-direction in a elastic beam
beam_ne = beam_ez*beam_ex;  % Total number of elements in elastic beam
total_area = 0; total_astr = 0; max_stress = 0; % Initial values

aa_cal_are = 0; aa_cal_str = 0; % "area_avg_calculator" for use with
for ix = 1:(floor(beam_ex*0.8)) % Calculation is performed for 80% of the elastic beam
    for iz = 1:beam_ez
        cr_x = ord_fix(beam_nd(ix:(ix+1),iz:(iz+1),1));
        cr_z = ord_fix(beam_nd(ix:(ix+1),iz:(iz+1),3));
        st_1 = ord_fix(beam_st(ix:(ix+1),iz:(iz+1),1));

        for ip = 1:4
% Area and stress calculation using four nodes
            ip_area = (cr_x(ip)*cr_z(1+mod(ip,4))-...
                cr_x(1+mod(ip,4))*cr_z(ip))/2; % Nth poly area algorithm
            ip_astr = (st_1(ip)+st_1(1+mod(ip,4)))/2;%
```

Algorithm A.3. Continued

```
          max_stress = max(abs(st_1(ip)),max_stress); % Maksimum stress
           total_astr = total_astr + ip_area*ip_astr;
           total_area = total_area + ip_area;


       end
        % Area average of stress:
       [n_area,n_avgs] = area_avg_calculator2...
          (cr_x(1),cr_z(1),st_1(1),cr_x(2),cr_z(2),st_1(2),...
          cr_x(3),cr_z(3),st_1(3),cr_x(4),cr_z(4),st_1(4));
       aa_cal_str = aa_cal_str + n_area*n_avgs;
       aa_cal_are = aa_cal_are + n_area;
   end
end;
dist_astrsd = -abs((aa_cal_str/aa_cal_are)/max_stress) % Strain distribution
mean_astrs = total_astr/total_area; % Average stress


  title(['Nodes&Disps, contour is ply-str and sum-str and cal-str = ',...
char(26),num2str((aa_cal_str/aa_cal_are)/max_stress)]
```

Algorithm A.4. Tip deflection of cantilever beam in static form

```
FEAP * * Tip Deflection of Cantilever beam in Static Form

0 0 0 3 6 4                ! 3d

PARA

 l = 100                   ! Length of the beam

 b = 20                  ! Breadth of the beam

 hd = 40                   ! No. of elements - Horizontal direction

 vd = 8                    ! No. of elements - Vertical direction

 t  = (hd+1)*(vd+2)/2



BLOC 1

 CART hd vd

  QUAD 4

   1 0 0 0

   2 l 0 0

   3 l 0 b

   4 0 0 b



EBOUN

  1 0 0 1 1 1 1 1 1        ! Fully restraining all dof

CFORC

Node  l 0.0 0.0 0.0 -10000 0.0 0.0 0.0 0.0  ! Load of 1000kN and Y-direction
```

Algorithm A.4. Continued

```
MATE 1
 SHEL
ELAS ISOT  69.0e+6  .330e-0
 THIC,,  2                    ! Shell thickness


END


BATCH
  TANG,,1
  DISP,,t
  STRE,t
  REAC,t
  plot mesh
  plot node
  plot boun
  plot load
  FORM
END
INTE
STOP
```